12-2017

Developing Algorithms for Quantifying the Super Resolution Microscopic Data: Applications to the Quantification of Protein-Reorganization in Bacteria Responding to Treatment by Silver Ions

Sai Divya Challapalli
University of Arkansas, Fayetteville

Developing Algorithms for Quantifying the Super Resolution Microscopic Data: Applications to the Quantification of Protein-Reorganization in Bacteria Responding to Treatment by Silver Ions

A thesis submitted in partial fulfillment
of the requirements for the degree of
Master of Science in Microelectronics-Photonics

by

Sai Divya Challapalli
Jawaharlal Nehru Technological University
Bachelor of Science in Electronics & Communication Engineering, 2013

December 2017
University of Arkansas

This thesis is approved for recommendation to the Graduate Council.

Dr. Yong Wang
Thesis Director

Dr. Jiali Li
Committee Member

Dr. Timothy J. Muldoon
Committee Member

Dr. Rick Wise
Ex-officio Member

The following signatories attest that all software used in this thesis was legally licensed for use by Ms. Sai Divya Challapalli for research purpose and publication.

_____	_____
Ms. Sai Divya Challapalli, student	Dr. Yong Wang, Thesis Director

This thesis was submitted to http://www.turnitin.com for plagiarism review by the TurnItIn company's software. The signatures have examined the report on this thesis that was returned by TurnItIn and attest that, in their opinion, the items highlighted by the software are incidental to common usage and are not plagiarized material.

_____	_____
Dr. Rick Wise, Program Director	Dr. Yong Wang, Thesis Director

Abstract

Histone-like nucleoid structuring proteins (HNS) play significant roles in shaping the chromosomal DNA, regulation of transcriptional networks in microbes, as well as bacterial responses to environmental changes such as temperature fluctuations. In this work, the intracellular organization of HNS proteins in *E. coli* bacteria was investigated utilizing super-resolution fluorescence microscopy, which surpasses conventional microscopy by 10–20 fold in spatial resolution. More importantly, the changes of the spatial distribution of HNS proteins in *E. coli*, by addition of silver ions into the growth medium were explored. To quantify the spatial distribution of HNS in bacteria and its changes, an automatic method based on Voronoi diagram was implemented. The HNS proteins localized in super-resolution fluorescence microscopy were segmented and clustered based on several quantitative parameters, such as molecular areas, molecular densities, and mean inter-molecular distances of the k-th rank, all of which were computed from the Voronoi diagrams. These parameters, as well as the associated clustering analysis, allowed us to quantify how the spatial organization of HNS proteins responds to silver, and provided insight into understanding how microbes adapt to new environments.

Acknowledgements

I would like to express my deepest gratitude to my advisor, Dr. Yong Wang, for his continuous support and outstanding guidance throughout my Master's degree. I would also like to thank Dr. Rick Wise, for his patience and best suggestions towards the completion of my Master's degree.

With the deepest thanks, I would like to thank my family and my parents, Challapalli Sreenivasa Rao & Challapalli Sarada Devi, who raised me and for their continuous encouragement and endless love. Without their support, I might not be the person I am here today. And most of all, I thank my beloved husband Haragopal Kambhampati who was there beside me during my graduate school challenges and my entire life. I am very happy to have you in my life. I am also thankful to my parents-in-law, Kambhampati Subrahmanya Sastry & Prabhavathi, for understanding me.

Dedication

To my husband and parents.

Table of Contents

List of Figures

List of Tables

1. Introduction

Silver used as antibiotic agent:

Silver plates were initially used to treat and prevent infections. Silver was the most important metal used by ancients after gold and copper. Silver was used to cure various medical infection even before the introduction of antibiotics in the 1940s, unaware of the fact that microbes were cause of infections. Silver preparations were used to treat and cure ulcers and in the process of healing wounds. Greeks, Russian, Romans and Egyptians used silver in one form or other. In early days when there was no refrigeration, silver containers were used to preserve milk and water [1] . Silver coins were dropped in the transportation containers for preserving and preventing the spoilage of milk and water [1]

To support the discussion that silver was used to suppress the growth of bacteria, research was performed in the year 2000 to analyze the outcome of silver ions on Escherichia coli and, Staphylococcus aureus [2]. From the studies, it was evident that silver ions had an impact on the bacteria growth. Microbes are present everywhere in the world and microbes are various types of viruses, fungi, bacteria, and pathogens [3]. Most of the microbes are harmless and some of the strains of the bacteria cause serious infections in plants, animals and humans [3]. To cure infections antibiotics are used, but bacteria is gaining resistance to the antibiotics. The resistance of bacteria to antibiotics is due to transformation in chromosomes and genetic materials through plasmids and transposons and, as time passes, bacteria gained resistance to the antibiotics [4]. Because of this, the number of new antibiotics that are being developed and approved has steadily decreased in the U.S. [5]. There is a need for the development of new antibiotics to treat the drug resistant bacteria [5]. Silver ions show a promising result in suppressing the growth of bacteria and are studied on *E. coli* bacteria.

1.1. Introduction to Histone Like Nucleoid Structuring Proteins

1.1.1. *E. coli* Bacteria

Theodor Escherichia first found *E. coli* in the year 1885 while he was investigating the feces of newborn babies and is known as Bacterium Coli commune, now called Escherichia Coli [6]. Escherichia, also called *E. coli,* is part of the large bacterial family and is a gram-negative rod-shaped microorganism which can be grown on gelatin or agar medium [6]. The size of *E. coli* bacteria is 2 μm long, with 0.5-2 μm diameter and volume of 0.6-0.7 μm^3 [7]. This is the common species which is being significantly studied and has become a typical structure in the field of microbiology. *E. coli* is the perfect model as it is simple and has a fully sequenced genome. Conventional optical microscopy can be used to look at *E. coli* and a detailed structure of the bacteria cell can be obtained by using the super resolution microscopy [8]. In the year 1886, *E. coli* was explained in detail jointly with another essential organism known as Bacterium lactis aero genes [6]. Resemblances of *E. coli* and Bacterium lactis aerogenes to Salmonella typhi indicated that *E. coli* are a harmless saprophyte [6], but in 1935 it was discovered that *E. coli* were the reason for outbreak of diseases such as diarrhea in newborns [9]. Generally, the strains of *E. coli* do not cause any harm, except a few strains are sources for severe diseases and infections such as urinary tract infections, gastroenteritis, and even food poisoning [9].

Habitation of E. coli:

E. coli habitat natively inside the human intestine and another craniate. In 1929, Bulloch proposed that strains of *E. coli* can live outside on animal bodies [6].

Temperature Resistance:

When exposed to a temperature of 55 ^{o}C, *E. coli* can be easily cultured in the laboratory for research [6]. *E. coli* strains can be grown at 37 ^{o}C and, under certain optimal conditions, *E. coli* can grow or reproduce in 20 minutes [6]. In research laboratories, *E. coli* bacteria are grown

in different mediums such as LB broth (lysogeny broth) which contains glucose, ammonium phosphate, potassium phosphate, and sodium as a medium [6]. *E. coli* bacteria respond to changes in the environmental conditions such as a change in pH levels and temperature [6]. For instance, *E. coli* can detect the changes in their surroundings such as increases in gas level and attempt to escape from the gases [9]. In correspondence to temperature fluctuations, the pore size of the outer membrane can vary accordingly, to either absorb nutrients or exclude them [9].

1.1.2. HNS Protein

Disparate groups of polypeptides are formed by the nucleoid–associated proteins. In *E. Coli*, while 12 of the polypeptides have been recognized as nucleoid–associated, most of the research is carried out on Histone-like nucleoid structuring protein (H-NS) [10]. H-NS protein is the abundant protein in the *E. coli* and in intimate groups of bacteria. There is another protein known as StpA, which has an analogous molecular mass, but when compared to H-NS protein it is significantly less ample. H-NS protein has been studied for years in *E. coli* bacteria, which is accompanied with the bacterial chromosome. The molecular weight of H-NS protein is 15.6 kDa and is also well-known as H1a protein. Gene regulation and DNA folding in the bacterial cells function with the help of the H-NS protein [11]. Hence, it also performs a significant role in the movement of the bacteria and led to the name, histone-like nucleoid structuring protein [12], because it not only binds to the DNA but also has an important RNA binding activity. In addition, it is considered a nucleoid related protein as well as a transcriptional repressor [13]. H-NS is being used in many other biological developments as well [12].

H-NS Structure:

it is critical to understand the function of H-NS protein. The H-NS protein contains two domains: A C-terminal and an N terminal domain which help in DNA-binding and

oligomerization process [12]. When H-NS protein comes in contact with the DNA it acts a dimer. DNA binding activity is minimized when the oligomerization domain is condensed [12]. DNA plays an important role in analyzing the functions of H-NS proteins, so it is important to understand the DNA binding methods and arrangements [14]. H-NS protein is compatible with all the nuclei acid and it binds firmly to double strand DNA [14]. The typical characteristics of the H-NS protein is it consists a three-dimensional DNA domain, which is not like other DNA binding proteins [12]. The DNA molecule rigidity is increased when the HNS protein binds to the DNA molecule. The DNA molecule rigidity transforms upon the type of buffer composition [12]. H-NS protein binding to DNA was shown in Figure 1.

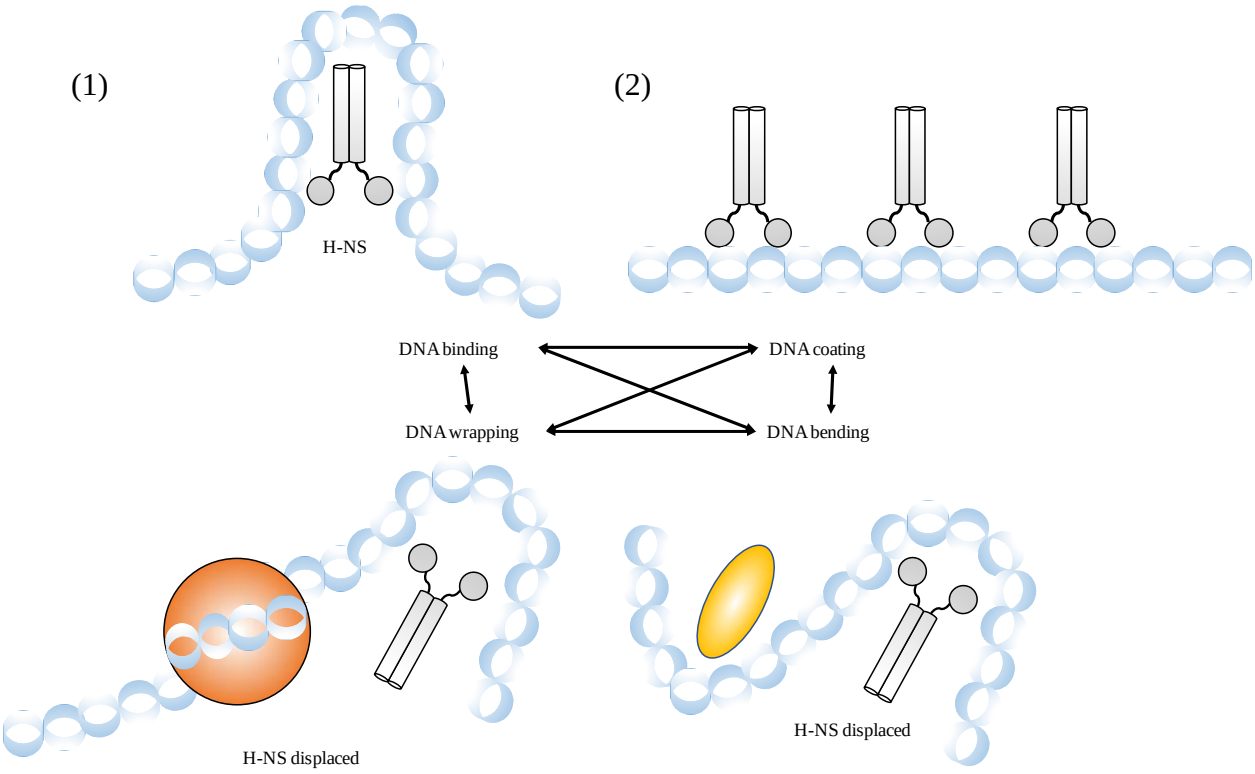

Figure 1. H-NS protein binds to the DNA and changes the DNA structure. The protein binds to the DNA in different forms: (1) DNA binding where H-NS protein attaches to the two sites of DNA that are apart from each other and forms a loop (top left); (2) the protein binds to two parts that are on a similar strand resulting in DNA coating upon it(top right). A DNA wrapping (bottom left in orange color) or a DNA binding (bottom right in yellow color) protein can affect the reliability of the bridge [15].

Nucleoid modeling and gene expression functions are carried out when H-NS protein binds to the DNA [14]. Hence, the binding of H-NS to the DNA plays a significant role. A complete explanation regarding the binding structure is not accessible [11] [15].H-NS can bind to DNA on only one side resulting in DNA coating or it can bind to DNA at a far distance, resulting in DNA bridging. A DNA bending protein or a DNA wrapping protein can be destabilized by displacing the H-NS protein [15].

The H-NS protein controls the functions of the genes that control the stress and helps in the successful functioning of the bacteria [16]. It could be argued that addition of silver ions changes the structural gene and will result in changes in DNA conformation [16]. This helps in to understanding that H-NS experiences a structural transition, resulting in the formation of clusters. It is observed that density-based clustering is more accurate and efficient for larger clusters and clusters of uneven sizes [17].

1.1.3. MEOS Protein

Photoactivable fluorescent proteins (PAFPs) are used in super resolution microscopy for imaging. Monomeric (m)Eos2 is an engineered photoactivable fluorescent protein that is generally utilized for this purpose [18]. Eos was initially isolated from the Lobophyllia hemprichii [19]. Eos can also be called EosFP, which stands for photoactivable fluorescent proteins.

The ability of the super resolution microscope depends upon the features of the photoactivable fluorescent proteins. EosFP emits a green emission and red emission at the peaks of 516 nm and 581 nm [19]. Eos is a wild-type tetrameric protein [19]. The practice of using PAFPs depends upon qualities such as size, brightness, oligomer nature, rational rate, maturation rate, photon ability to switch at different rates, and the pH level [18]. The tetrameric nature of

EosFP is solved by developing numerous monomeric forms such as mEos2, mEos3.1, and mEos3.2 [18]. In comparison with mEos3.1 and mEos3.2, the mEos2 is preferred as it gives overall better performance [18].

The disadvantage of using mEos2 is that at higher concentrations it forms dimers as well as oligomers [18]. This has limited its applications for labeling membrane proteins at higher concentrations. Hence, the use of mEos2 is limited to mammalian cells [19]. This problem can be overcome by developing monomers mEos3.1 and mEos3.2 [18]. The photoactivatable proteins possess fluorescent characteristics which can be controlled by illuminating them with radiances of a specific wavelength, duration, and intensity.

The monomeric forms of Eos are used for labeling the cells that help in successive analysis to observe the kinetics and operating of the single molecule [18]. Eos undergoes irreversible photo conversion in response to a wavelength of 390 nm light. The properties of Eos are listed in Table 1.

Table 1. Properties of Eos.

Red absorption peak	571 nm
Red emission Peak	581 nm
Green absorption peak	506 nm
Green emission peak	516 nm
Green luminosity	1.3X
Red luminosity	0.7X
Wavelength of photo conversion factor	390 nm

1.2. Introduction to Single Molecule Localization Microscopy

1.2.1. Single Molecule Localization

Organic dyes and fluorescent proteins enhance the utility of the microscope, which improves the ability to understand proteins, DNA, and organelles structures. However, diffraction, which is the major problem, has made it difficult to observe objects which are less

significant than the diffraction limit, i.e., 250 nm. This can be overcome by using a technique called FIONA (Fluorescence Imaging with One Nanometer Accuracy) [20] . The FIONA technique is straightforward yet valuable procedure for localizing single fluorophore [20]. This method is used to localize the position of a dye in the x-y plane within 1 nm and the location of a diffraction-limited spot is positioned within a few nanometers [20]. It works on a principle of choosing the point spread function of a single fluorophore, finding the focal point of the fluorescent spot with the help of two-dimensional Gaussian fit, and exciting the single fluorophore using wide field illumination [20]. An image captured by a camera comprises several background elements such as noise, fluorescence setting, camera readout, the result of pixilation and even photon noise; Equation 1 allows calculation of the resolution of the image. [20]. All these features can be reduced by gathering more photons.

$$\sigma_{\mu_i} = \sqrt{\left(\frac{s_i^2}{N} + \frac{a^2/12}{N} + \frac{8\pi s_i^4 b^2}{a^2 N^2}\right)} \qquad \text{(Equation 1)}$$

The main aim is to define the center or mean value of the distributions $\mu = (x_0, y_0)$ σ_{μ_i} is standard error of mean, index i represents x or y-direction, N is the photon count, s represents standard deviation of fluorescent spot, a estimates the pixel size, and b is background standard deviation [21]. 1 nm precision can be achieved for a fluorophore emitting ~10,000 photons using FIONA technique [21]. The initial term $\frac{s_i^2}{N}$ expresses photon noise, the second term is the finite pixel size effect of the detector and the following term accounts for background noise. FIONA helps in determining the spot of both static or moving particles. The motion of the single molecule can be tracked even from movie frames using FIONA [21]. Additionally, fluorescent objects with different sizes, lengths, and diffraction limits can be tracked and analyzed using FIONA and can produce a center of mass with an accuracy of a nanometer [21]. Localization precision issues up to one nanometer can be resolved by using FIONA and localization precision

is improved significantly. An introduction to TIRF, the equipment setup for carrying the FIONA technique, and total internal reflection fluorescence microscopy (TIRFM) [21], are explained in the next section.

1.2.2. TIRF Introduction

Total Internal Reflection Fluorescence (TIRF) helps illuminate the selective fluorophore in mediums which are near to the glass or any interface. TIRF helps in the visualization of the cells. The fluorescent samples can also be imaged using the TIRF technique. Other techniques in the presence of fluorescence obscure the image when it meets the regions. TIRF helps in qualitatively observing the sample position, movement, composition, and the contact regions. It also helps in measuring the concentration, binding, equilibrium, distance from the substrate, and kinetic rate of the biological surfaces.

The concept of TIRF is relatively simple and can be implemented on both conventional upright or inverted microscopes where lasers can be used as a light source [22]. A light beam traveling through the glass surface is incident at angle θ where the cells are attached to the surface of the solid or liquid medium. The angle θ measured must be such that the beam must be large enough to totally internally reflect through the interface [22]. This condition takes place beyond the critical angle. TIRF generates a field known as the evanescent wave. The evanescent wave is generated by a narrow electromagnetic field in presence of liquid with similar incident light incidence and exponentially decays in intensity as the distance from the surface increases [22]. The evanescent wave helps in exciting the fluorophore nearer the surface of the liquid. It does not illuminate the fluorophore beyond the liquid medium [22]. To setup a TIRF microscope, various elements needed, including for the alignment process, are listed in Table 2.

Table 2. Materials needed for TIRF set-up [21].

Optical table
Laser 532nm, 30mw.
XYZ translation stage
Optical beam
ND filters
Laser safety goggles
Alignment target
10X beam expander
1” diameter broadband dielectric mirrors with mounts
2” diameter broadband dielectric mirrors with mounts

All the mirrors and lenses must be the anti-reflective equivalent of the laser being used. It must be ensured that the elevations of all optical components match the center of microscope back port. The laser and laser shutters along with the ND filters are fixed with the help of screws. Neutral density (ND) filters help in reducing the laser intensity and, at the same time, make the beam visible. A beam path on the optical table using an indicator must be designed as shown in Figure 2. The mirrors and position mirror M1 must be mounted at a right angle. A dichromatic mirror and two irises must be positioned along the beam path. The mirror M1 must be adjusted in a way that the laser hits the dichromatic mirror and passes through both the irises. Mirror M2 is placed at a second right-angle. The position of the mirror is adjusted such that it follows the beam path of mirror M1. Another mirror M3 is situated in front of beam expander (L1 & L2) with magnification 10X [21]. The mirror M3 is adjusted with the goal that the laser beam goes through the focal point of L1 and L2. The beam expander should be lateral to the optical table and the beam path [21]. Mirrors M1 and M2 are adjusted repeatedly so that the laser passes within the center of the two irises and the lenses of the beam expander. The output of the beam should not be clipped.

If the laser is clipped, then it indicates that it is a bad beam. The beam profile can be checked by placing a white paper after the beam expander. Higher precision analysis can be

obtained by using optical fiber. The beam size does not get altered by distance. The space between L1 & L2 is altered in a way that the beam is gathered. The microscope objective is removed and a fluorescent alignment target is screwed in. Mirror M3 is used to direct the laser beam into the beam expander (L1 & L2). The expanded beam is pointed inside the microscope port and on the dichroic mirror. The laser beam reflects off the dichroic mirror in the direction of the ceiling. If the alignment is done properly, the symmetric spot can be observed reflecting on the objective. Then, the TIRF lens (L3) is positioned on the XYZ transitional stage. It is placed just before where the light is incident on the microscope and adjusted such that it is reflected properly. The materials and setup of TIRF microscopy is showed in the Figure 2.

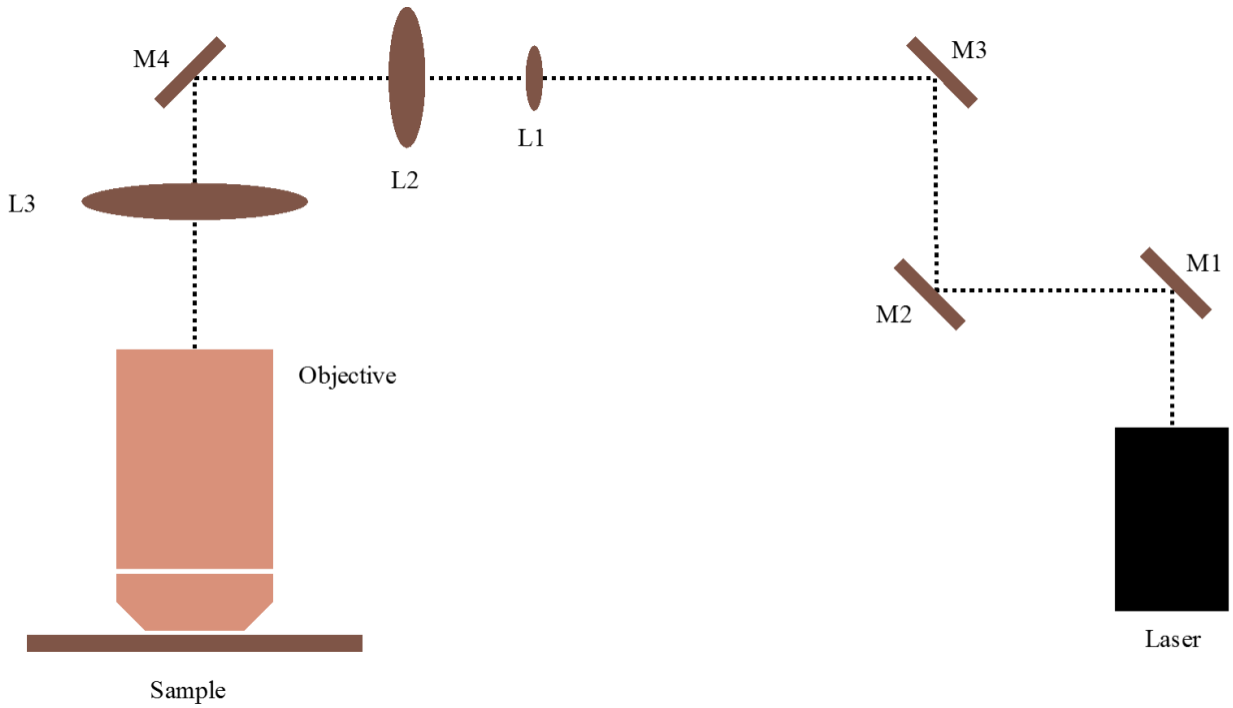

Figure 2. Setup for total internal reflection fluorescence microscopy (TIRFM). L1, L2, and L3 are the lenses and M1, M2, M3, and M4 are the mirrors [21].

1.2.3. Comparison of TIRFM with other Optical Microscopes

TIRFM is the optical technique widely used in many microscopes such as confocal,

multiphoton, and interference reflection contrast [22]. All the techniques have advantages and difficulties. In confocal microscopy, axial selection is achieved with the exclusion of out-of-focus radiated light, but confocal microscopy is flexible and its technique of optical sectioning can be used on the plane of the sample (i.e. this is the added advantage) [22]. Nevertheless, by using TIRFM, the disadvantages in other optical microscopes such as confocal microscopy can be overcome.

The optical section depth in confocal microscopy is as thick as ~0.6 μm while in TIRFM it is ≤ 0.1 μm [22]. Confocal microscopy is expensive when compared to TIRFM. TIRFM can be used with any regular microscope, can be interchangeable even with a home built microscope, and is less expensive. Nowadays, arc and laser established TIRFM are available on the market and from third party suppliers. TIRFM was initially used for macroscopic applications rather than microscopic applications. TIRFM speed does not depend upon hardware or image reconstruction software. TIRFM is well-suited with epifluorescence, bright-field, dark-field, or phase-contrast illumination so these strategies of light can be swapped back and forward promptly [22].

Optical microscope:

Optical microscopes use visible light and lens to magnify images of small size [23]. The optical microscope resolution is defined by the point spread function (PSF). The PSF indicates the reaction of the point-like object, such as the single fluorescent emitter that makes the image appear larger than it is [23]. Abbes diffraction formula for lateral (i.e. XY) resolution is given by $d= \lambda/2(\theta)$, and axial (i.e. Z) resolution is given by $d= 2\lambda n/(\theta)^2$ in the focal plane and near the optical axis [23]. λ represents the wavelength of light, the refraction index of the medium is given by n, and θ is the numerical aperture (NA) of the objective lens [23]. The latest super

resolution techniques try to overcome this limitation to obtain high-quality structural images.

1.2.4. Introduction to Super Resolution Microscopy

In the field of biological studies, fluorescence microscopy is one of the most popular and multipurpose techniques [23] . With the help of fluorophore-labeled molecules, it is very easy to obtain a good quality or high resolution image, as these fluorophores are very bright and can be easily distinguished from other particles or signals [23]. The innovation of super-resolution microscopy has increased the chances for scientists to image the individual cell, their internal dynamics, localizations, and almost all the activities in the living cell. It has opened the doors for the scientists to come up with new and exciting questions and challenges in the field of microbiology [24].

With the advancements in super-resolution microscopy, it is quickly growing as a commercial tool. In any case, super-resolution microscopy is not confined to any individual technology. Depending upon the field of interest, different technologies are implemented. However, the optical microscope spatial resolution is minimal because of the nature of the light [23]. The resolution of the light microscope is controlled by the properties of the light diffraction as stated by Ernst Abbe in 1873 [23]. The resolution of the light microscope is ~250 nm in the x and y direction and is greater than 450-700 nm in the z direction [24]. The light microscope resolution limit depends upon two main aspects: light wavelength and the numerical aperture of the objective lens [23]. The resolution is described by evaluating the point spread function (PSF) [24], an easy method to distinguish resolution. PSF can be described as the stable size of the spread of a point of light through a microscope which is being diffracted [24]. “Resolution” means the ability to identify the adjoining objects as an individual structure, not as a single object, hence the word “resolution” does not mean the capability of a microscope to

detect the smallest objects (see Figure 3) [24] .

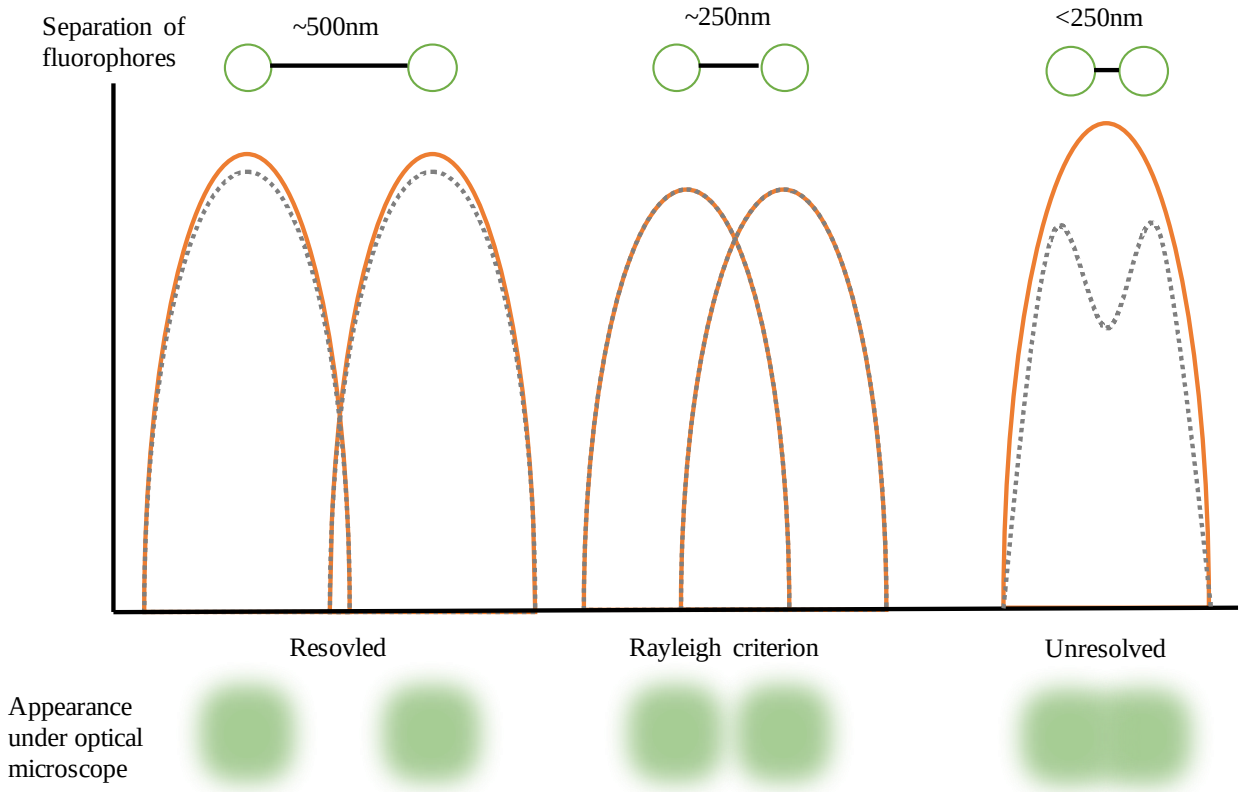

Figure 3. Optical microscope resolution estimation. The optical microscope is used for resolving point like sources only if they are separated by the Rayleigh criterion. If the point like objects are closer together than 250 nm, they cannot be resolved [23].

Though the objects are smaller in size than PSF and are nearer to each other when compared to the width of PSF, these objects cannot be identified as separate objects under the microscope [24]. The PSF width can be measured by using the Rayleigh criterion. In 1896, Rayleigh defined the Rayleigh criterion, $R = 0.61\lambda / NA$, as the minimum distance where two-point emitters are identified as individual things [23]. By this, it can be understood that the diffraction of light restricts the resolution of the microscope, so the finer structures of any cell cannot be determined [23]. The microscope which can overcome the diffraction limit of the conventional light microscope is considered a super resolution microscope. Super resolution

techniques overcome the limitation of the light diffraction partially or spatially by modifying the activation light [24]. In recent years, with the development of different fluorescence microscopy, different super-resolution procedures have been developed. Super resolution microscopes are not confined to a single method; hence, several methods have been developed over a period for super resolution fluorescence microscopy. These include SIM (structured illumination microscopy), STED (stimulated emission depletion) microscopy, PALM (photo activation localization microscopy) and STROM (stochastic optical reconstruction microscopy) [23].

All the techniques mentioned can overcome the diffraction limit and are unique when compared with each other. Each technique, when applied in any field, has both advantages and disadvantages. Before trying to implement the super resolution techniques, one should give thought to the following important issues: What is the amount of resolution needed to reveal the object? What is the speed needed? Can the live cells be illuminated? What would be the size and density of the object? Can the sample be labeled by using dyes or fluorescently tagged proteins? [23]. Specific microscopes are not manageable, particularly while illuminating organic samples [23]. Hence, one should be careful while choosing a method by considering both the strengths and weaknesses of the technique and how useful it is based on requirement [23]. Table 3 describes the differences between super resolution techniques.

Table 3. Comparison of super resolution techniques [23].

	SIM	STED	PALM/fPALM	STORM/dSTORM
Resolution (X, Y)	100-130 nm	20-100 nm	20-50 nm	20-50 nm
Z axis resolution	250-350 nm	560-700 nm	100 nm (TIRF)	100 nm (TIRF) 20-30 nm (3D STORM)
Illumination	Wide field (epi/TIRF)	Laser scanning confocal	Wide field (epi/TIRF)	Wide field (epi/TIRF)
Types of probes	Conventional fluorescent probes	Conventional fluorescent probes	Photo-activable fluorescent proteins	Photoswitchable dyes
Time for acquisition	In seconds	In seconds	In minutes	In minutes

Table 3. (Cont.)

	SIM	STED	PALM/fPALM	STORM/dSTORM
Post-acquisition processing	Yes	No	Yes	Yes
Energy intensity	Intermediate	Intermediate - high	Intermediate - high	Intermediate -high
Imaging of vital cells	Restricted (2d-TIRF)	Restricted	Restricted	Restricted
Simultaneous colors	3	2	2	2

1.2.5. Probe Selection for Super Resolution Microscopy

When compared with other fluorescence microscopy techniques, the selection of fluorescence probes in super resolution imaging plays an important role. All the techniques use a different kind of fluorescent probes depending on the requirement. The only super resolution technique like the basic fluorescence microscopy that does not require any special probe is the SIM technique [23]. All other super resolution microscopy techniques, such as PALM and STROM, require fluorescence probes which can be controlled reversibly or irreversibly so that they can be switched between light and dark states [23]. Bright probes are preferred for high contrast ratio among the two states [23]. When compared with other techniques, STED cannot be used with the conventional fluorophores because of the depletion selection limit. This indicates that the red fluorescent proteins and dyes are a challenge for dual color imaging [23]. The STROM requires a couple of dyes. Nevertheless, still, there is a need for the development of the probes to increase the number of color choices.

Acquisition Speed:

The resolution of the super resolution technique can be improved by improving the speed of image acquisition cost, as it uses the hardware of conventional microscopy [24]. The resolution of STED microscopy is approximately 35 ms, with an image view of 1.8 μm to 2.5

μm within the field of view and 62 nm resolution at a 2D resolution [24]. Less time is needed to scan a larger PSF when compared to scanning the smaller PSF [24]. While acquiring images, it is essential to know whether the biological sample changes with respect to the time scale when selecting a suitable super resolution microscope. The switching between speed and resolution is more pronounced while using single-molecule localization techniques such as PALM and STROM [24]. At any given time, two molecules cannot be turned on within the same PSF. The super resolution image can be captured by repeatedly switching on and off the fluorophores. When compared to the localization precision, the spatial resolution is comparatively less. While imaging live cells using the single molecule technique, the sampling should be fast enough to avoid the blurring of the images.

STED (stimulated emission depletion) is the fastest super resolution technique. The STED technique is successfully used in the field of biology [25]. The selection of the right dye is important and its speed of acquisition depends upon the size of the field of view. If the field of view is small, it is relatively fast, and slow when the field of view is large. Imaging small fields of view is the good choice for the best video rate. Severe photo bleaching should be prevented to get good images. In recent years, two-color STED has been validated and is also available for use [25]. The extension to three color usage was not achieved due to the need for non-overlapping excitation, emission, and wavelength depletion bands [25].

1.2.6. Data Acquisition and Localization

Initially, the sample is prepared with suitable buffer solutions and temperature conditions. First, the regions of interest (ROIs) having radiation from fluorescent emitters are recognized [26]. This process is carried out by thresholding the raw frames depending upon the pixel intensity associated with background noise intensities [27]. The focus of ROIs utilized for

localization of the fluorophore is selected by pixels having values larger than the fixed threshold value [27]. Sophisticated segmentation algorithms are suggested for the selection of ROI regions so that the fluorescence signals from blob-like sources from the background intensity and noise are separated, by first decomposing the raw images into wavelet maps. Consequently, the ROI is identified by implementing watershed segmentation algorithm [28]. When the region of interest in the raw data has been identified, the position of emitting fluorophores in these regions is evaluated. Samples with appropriate fluorophores are stimulated using the right laser wavelength. The intensity of the lasers is adjusted until an optimum level of fluorophore stimulation is identified with the appropriate density. Most of the photo switchable fluorophores able to be transitioned from a dim state to a fluorophore state with the help of activation lasers [28]. Lastly, the fluorophore time switching captures hundreds to thousands of discrete subsets of image frames individually emitted from the unique subset of the groups.

The next step is filtering the raw localizations so that it eliminates localizations that are not in the right position. For instance, multiple fluorophores might be emitted by overlapping, auto-fluorescence, and residual contamination. The process of filtration is carried out based on the results from the localization algorithms such as fluorophore intensity, PSF width, localization precision, and the information or data about the presence of fluorophores. This process is carried out so that the super resolution images are not formed by both finely and inadequately localized molecules. Finally, the localized molecules from each image are combined to form a super resolution image.

1.2.7. Super Resolved Images

Once the imaging data is acquired, hundreds of thousands of single images frames are obtained. The acquired data frames have points of intensity equivalent to the intensity of light

produced from the attached fluorescent label [29]. The position and location of fluorophores are identified in each frame and a complex image is formed. The complex picture helps us to identify the location of the fluorophores during imaging. Each single molecule location is identified to locate the fluorophore location. This process is completed by selecting the required threshold to differentiate the signals coming from each of the fluorophores with respect to the background [29]. When the signal is high enough, target fluorophores are identified. When the target fluorophore is recognized, the signal is attached to a 2D Gaussian distribution. In single molecule localization images, single fluorophore images are considered small Gaussian intensities whose width is scaled according to the precision of the fluorophore [29]. After imaging the single molecule, imaging data is processed using ImageJ software [30]. Drift correction is an important step to obtaining accurate results.

The sketch in Figure 4 helps explain the process of single molecule imaging in a better way. A circle like object has a smaller diffraction resolution and is labelled with switchable fluorophores. By switching on and off the molecules are activated and the structure is labeled. This process helps to overcome the sub-diffraction limit. By activating the molecules and imaging them consecutively the position of individual molecule is determined. The yellow color circle represents the fluorescent image and the center of the image is marked in blue color + symbol [31].

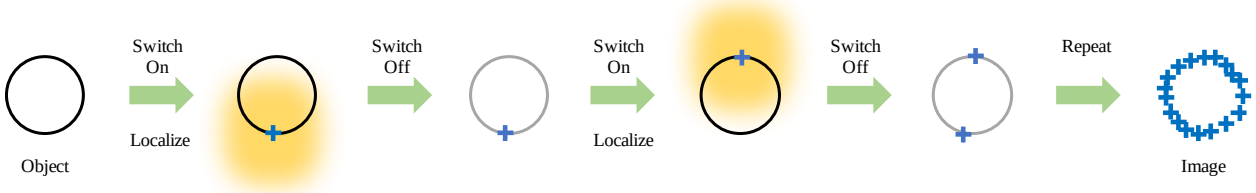

Figure 4. Illustration of imaging fluorophores covered sub diffraction limited objects by sequential activation.

1.3. Introduction to Cluster Analysis Algorithm in Super Resolution Microscopy

One of the most widely-used data analysis techniques is cluster analysis [32]. It assists the operator in realizing the grouping technique in a data set. Larger volumes of stored databases are analyzed using the cluster analysis technique. The need to analyze large amounts of data is increasing day by day. Consequently, clustering algorithms are widely being used in the past few years [32]. Typically, the clustering algorithms work on the principle of grouping objects in each database for subsets, groups, and classes. After the partition, the clustering groups should possess the conditions of homogeneity within the cluster and heterogeneity between the clusters, i.e., data that belong to the same cluster must be as related as possible and data from different clusters data must be as diverse as possible [33]. In general, all the clustering algorithms require input parameters which, in some cases, might be difficult and have the impact of clustering results [32]. The efficiency of clustering algorithms depends upon three main reasons. Initially, most of the clustering algorithms need input values. Second, the input parameters are very discreet to the given parameter values [32]. Different partitions of the datasets are formed, even though the parameters are slightly off the diverse settings. Thirdly, high dimensional data sets cannot be acknowledged by the clustering algorithms; with the help of global parameter settings, they alter the scattering [32].

Clustering algorithms are of two types: partitioning and hierarchical algorithms [34]. Partitioning algorithms require input parameters such as the domain knowledge and, unfortunately, most of the applications do not exist. Partitioning algorithms work on a principle of partitioning the database, D, of p objects into a set of clusters, K. The input parameter in this case is K [35]. The algorithm initially partitions D and then enhances an objective function by using an iterative control strategy [34]. Partitioning algorithms require two steps. Initially, the K representative must be determined by reducing the objective task [34]. Finally, each object is

allocated to the cluster object [34]. From the final step, one can determine that the partition is a Voronoi diagram and each individual cluster is present in one of the Voronoi cells. Hence, all the clusters identified in the process of partitioning algorithm are convex [34]. Therefore, the usage of partition algorithms is limited [34]. Hierarchical algorithms decompose the given data base, D, of objects, p, into smaller subsets so that each subset contains an individual object which is represented by a dendogram, i.e., a tree that iteratively splits D into smaller subdivisions.

1.3.1. DBSCAN Algorithm

Density-Based Spatial Clustering of Applications with Noise (DBSCAN) is an algorithm which uses a complementary technique for identifying clusters even in the presence of noise cluster [36]. It uses a density of points as a method to differentiate the clusters; the data sets that are dense are grouped and connected to form a single cluster [36]. It works on the basic principle that for every point of the cluster the density of the data points in that region must exceed the minimum threshold [37]. DBSCAN algorithm needs only two parameters as input, i.e., the cluster's least radius (r) and the least number of minimum points (M points) essential to form clusters [38]. To identify a new cluster or the neighboring clusters, the algorithm first checks whether the given set of data points meet the initial conditions that are set by the algorithm. The conditions set by the algorithms are given in Equation 2 [38]:

$$\text{Neighborhood } r\,(Xi) \geq \text{Minpts where } xi \in X \qquad \text{(Equation 2)}$$

where r is defined as the minimum radius of the cluster, Minpts is the minimum number of points required to form a cluster, X is a data set, and xi is each sample in the data set.

The DBSCAN algorithm divides the special localization of points into three types, namely, core localizations, border localizations, and noise [38]. The advantage of using this

algorithm in comparison with other segmentation-based algorithms, the DBSCAN algorithm has exhibited greater sensitivity, and segments several clusters even in the presence of noise [38]. The DBSCAN algorithm helps in identifying the arbitrary shapes and sizes of clusters and is even efficient for large databases. Basically, the DBSCAN algorithm was introduced to detect clusters in three-dimensional data. More recently, it has been used for distinguishing several other data structures. The applications of the DBSCAN algorithm are as follows: in the field of network traffic (to efficiently recognize sets of traffic that are alike [36]), in grouping single particle mass spectra in spectroscopy [36] and in classifying medical images While identifying clusters of small and moderate data arrays the DBSCAN algorithm is comparatively fast [36]

1.3.2. Ripley's K-function

The spatial organization provides us with information about the object's interface, organization, and chemistry. The identification of spatial distribution patterns can be done using two methods: the correlation method or threshold-based method. In correlation-based functions, there are two commonly used methods which are the pair correlation function (PCF) and Ripley's K-function [39]. The distribution of molecules can be evaluated analytically using a standard tool called Ripley's K-function [40]. Ripley's K-function helps in analyzing various types of protein clusters, domain size, and area. It is used to compute all the points in the lattice regardless of whether they are inside or outside the region [41].

Ripley's K-function is classically used to relate a given point distribution with a random distribution; i.e., the point distribution is verified in contradiction of the null hypothesis that the points are scattered arbitrarily as well as individually [41]. It provides the knowledge of the spatial patterns of the coordinates, how the single molecules are distributed, their uniformity and the size of the clusters [42]. The Ripley K-function is given as Equation 3:

$$K(r)= \frac{1}{n}\sum_{i=1}^{n} Npi(r)/\lambda \quad \text{(Equation 3)}$$

where λ represents the density of localizations and $Npi(r)$ represents the number points in the i[th] region at a distance r [43]. The value of K(r) can be projected for random Poisson distribution πr^2. The greatest challenge while using Ripley's K function is an identification of the point aggregation radius [41]. The K-function can be normalized so that the predictable value is linear r. L(r) and is given as:

$$L(r)= \sqrt{K(r)}/\pi \text{ [41]} \quad \text{(Equation 4)}$$

The normalized K-function yields to the H-function which is given as

$$H(r) = L(r) - r \text{ [41]} \quad \text{(Equation 5)}$$

The value of H(r) can be either positive or negative. The positive value indicates that the clustering can take place over the spatial measure, and depression indicates the negative value of H(r) [41]. The maximum aggregation of the radius is delivered using Ripley's functions. Hence, they are not useful for distinguishing clusters possessing heterogeneous shapes and sizes [43].

1.3.3. Pair Correlation Function

Pair correlation function, *g(r),* is defined as the possibility of finding the midpoint of a particle in each data set a given distance from the midpoint of another particle. The pairwise correlation function is also called the radical function [44].

In a simple way, it is a measure of the possibility of identifying a particle at a distance r from a reference particle [44]. Typically, the algorithm measures numerous particles that are at a distance *r* and *r + dr* away from a reference particle [44]. The function *g(r)* specifies how the density changes with respect to the distance from the reference point. The pair-correlation function helps in identifying the protein organization function, identifying protein clusters, and

the size, density and amount of proteins in the clusters [44]. The drawback of using the pair-correlation function is that localizations do not precisely display the marked molecules, due to localization vulnerability [45].

1.3.4. OPTICS Algorithm

The OPTICS (Ordering Points to Identify Clustering Structure) algorithm is a hierarchical clustering algorithm and is like the DBSCAN algorithm [46]. The parameter, e, in the DBSCAN algorithm is replaced by the maximum search radius. The OPTICS algorithm overcomes the drawback of the DBSCAN algorithm, which identifies clusters of different densities in each set of data. Large data sets can be analyzed by using the OPTICS algorithm. When compared to the DBSCAN algorithm, the OPTICS algorithm is not sensitive to the change in parameter values. The OPTICS algorithm helps the user to understand large data sets. OPTICS algorithm is used for analyzing the data in the fields of sensor databases and the emerging application areas [46]. The concept of the OPTICS algorithm is based on the core-distance and reachability-distance for objects with parameters Eps and MinPts.

Core-distance:

Consider a database D, and P is an object in the database. Parameters $\in$, $N_{\in}(P)$ and $MinPts$ are considered, where $\in$ is the distance value, $N_{\in}(P)$ is the neighborhood of P, $MinPts$ is a natural number, and $MinPts - distance(p)$ is the distance from p to its $MinPts$ neighbor [47]. The core distance of P is given as:

$$\in Minpts(p) = \begin{cases} Undefined, but\ card\left(N_{\in}(P)\right) < Minpoints \\ MinPts - distance(p), else \end{cases} \quad \text{(Equation 6)}$$

For an object, P, the core distance is considered the minimum distance $\in$ between p and

an object in its ∈ neighborhood, so that P will be a core object w.r.t to ∈ such that the neighbor is confined in $N_{\in}(P)$ or it is undefined.

Reachability distance w.r.t to object p to object o:

Consider a database D with p and o as objects. $Minpts$ is a natural number, $N_{\in}(o)$ is the ∈ neighborhood of o [47]. Then, the reachability distance of p with respect to o is defined as:

$$\in, Minpts\ (\mathrm{p},\mathrm{o})\ = \begin{cases} Undefined\ if\ |N_{\in}(o)| < Minpts \\ max(core - distance(o), distance\ (o,p)), else \end{cases} \qquad \text{(Equation 7)}$$

From object p, the reachability distance with respect to another object o is the minimum distance so that p is directly density-reachable from o when o is a core object [47]. If o is not a core object, similar at the generating distance ∈, the reachability distance of p with respect to o is undefined [47]. For an object p, the reachability distance differs based on the core object that is analyzed. Figure 5 illustrates the concepts of the core distance and reachability distance.

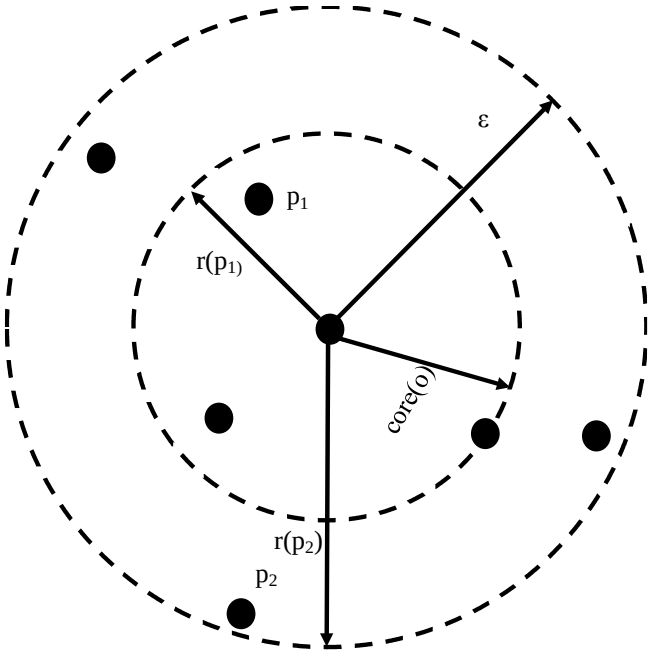

Figure 5. Reachability distance and core distance (o) [47].

1.3.5. The Voronoi Diagram

The Voronoi diagram is the most useful data analysis method in the field of computation and is used in many areas of scientific research. The concept is simple to understand, but is a logically interesting one and can be envisioned easily. Voronoi diagram is termed after Georgy Voronoi and is also known as the Voronoi tessellation, Voronoi decomposition, Voronoi partition, or a Dirichlet tessellation or tilings, Wigner-Seitz cells, and Thiessen polygons [48]. The Voronoi diagram is applied in many fields and is used in both theoretical and practical applications. The practice of the Voronoi diagram gradually emerged during the 1980s as observed by the above applications [49]. The major advantage of using the Voronoi diagram is that it can be simplified in many ways. The Voronoi diagram is a method of dividing a given set of points into several polygonal regions within the fixed set of points. Those points are called the Voronoi seeds. The formed polygon regions are called the Voronoi polygon and specify the number of surrounding seeds.

Initially, Voronoi diagrams already existed in nature in numerous circumstances and several cases can be used to describe modules of Voronoi diagrams [50]. Voronoi diagrams are one of the basic ways to construct a separate set of points. The capability of the Voronoi diagrams to solve computational problems has increased its applications in the field of computer science for solving various computational problems. Some of the applications are in anthropology, archeology, biology, computational geometry, crystallography, chemistry, ecology, forestry, geography, marketing, physics, phycology, statistics, and regional planning [49].

Fundamental Properties of Voronoi Diagram:

First, the basic definition of Voronoi diagram is explained. Consider a set, q, in a space,

S, with an object Pi. The Voronoi diagram of q is constructed by dividing the space into regions, R (Pi, q) such that R (Pi, q) contains all the points of S so that they are closer to Pi when compared to other objects, Pi, in S. Figure 6 shows the Voronoi diagram (general Voronoi diagram).

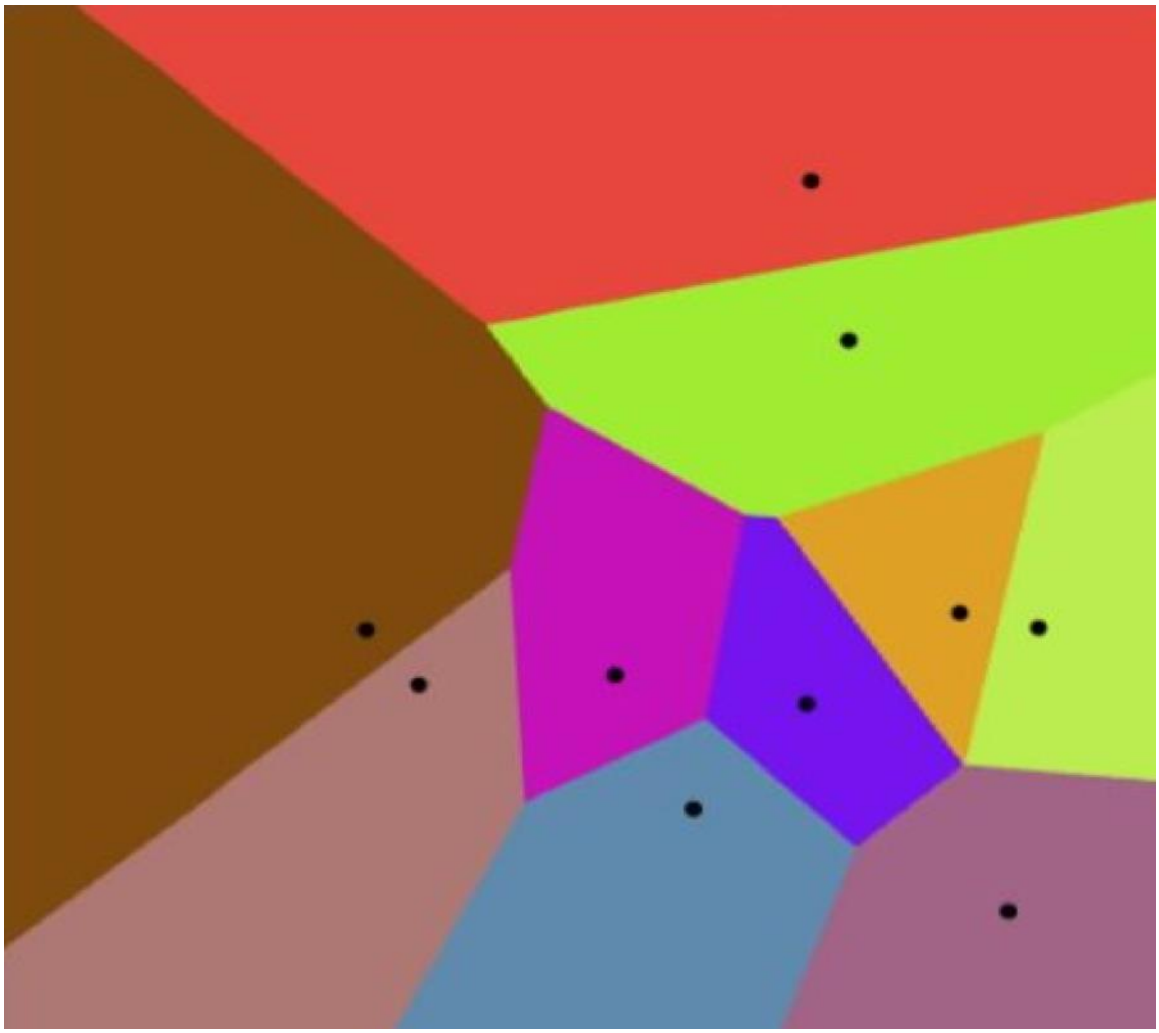

Figure 6. Illustration of Voronoi diagram. Black dots are called localizations or seeds. Colored regions are called Voronoi cells.

Each Voronoi region is produced by the intersection of n-1 half planes and the planes are called as convex polygon [51]. Hence, each boundary of a region contains as many as n-1 edges

and vertices as their end points [51]. Every point which is on the edge is equidistant from exactly two sites and the vertex is equidistant from at least three sites [51]. Hence, all the regions form a polygon-shaped plane or a polygon partition such that the regions are edge-to-edge and vertex-to-vertex [51]. The final figure is called the Voronoi diagram.

2. Experiments

Using silver ions, mechanistic studies were conducted on *E. coli* and gram negative Staphylococcus. Morphological changes occurred inside the bacteria cells after treating with silver ions. The effects were studied using electron microscopy and X-rays. The grouping of proteins was done using cluster and Voronoi analysis. To further understand the effects of silver on bacteria, experiments were conducted on *E. coli* bacteria using silver ions and were visually analyzed using super resolution microscope. The process is described in the following sections.

2.1. Sample Preparation for Imaging

2.1.1. Bacteria Growth, Cell Fixation, and Yield

The bacterial strain, K12DHNS+HNS-mEos3.2C1, was grown overnight at 37 ^{o}C in a M9 minimal medium, supplemented with 1% glucose, 0.1% casamino acids, 0.01% thiamine, and the appropriate antibiotics, Kanamycin and Chloramphenicol [52]. It is shown in the Figure 7. On the second day, the overnight culture was diluted into the fresh medium so that the optical density (OD600) of the medium measured 0.005 [52]. The total volume of each sample was around 15 ml. The fresh culture was again grown at 37 ^{o}C and the OD600 was measured every 20-30 min until the OD600 reached 0.2-0.4 (see Figure 7) Next, the growth conditions of the bacteria were changed by adding 1 mg/ml silver nitrate and the culture was incubated for another 30 min with orbital shaking. The cell fixation was done by adding 37% formaldehyde to the cell cultures so that the final concentration was 3.7%, and the culture was incubated at room temperature for 30 minutes followed by orbital shaking or manual shaking. The bacterial cells were harvested by centrifugation at 1000 g for 15 min at room temperature, followed by the removal of the supernatant (see Figure 8). The cell pellets were re-suspended by adding 1X PBS (phosphate buffered saline). They were mixed well for 5 min and centrifuged again at 1000 g for

10 min followed by the removal of the supernatant [52]. The sample was washed three times by resuspension in 1X PBS, centrifugation, supernatant removal, and the final sample was stored in PBS at 4 ^{o}C on the nutator. The sample was placed on the nutator to prevent the cells from precipitating out (see Figure 9).

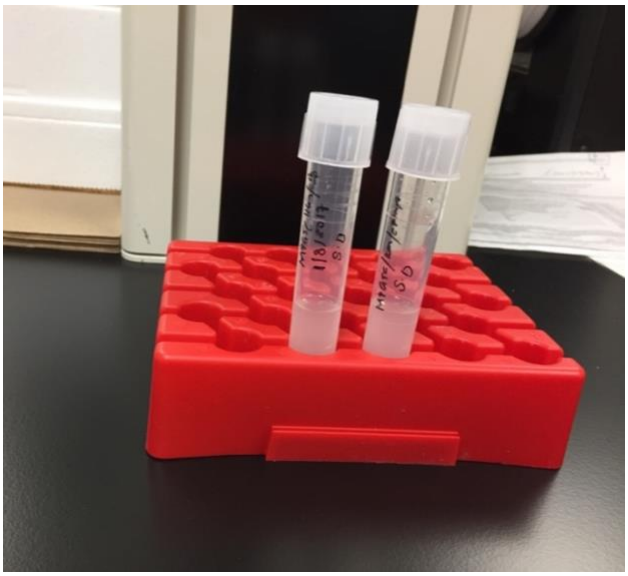

Figure 7. The bacterial strain, K12DHNS+HNS-mEos3.2C1.

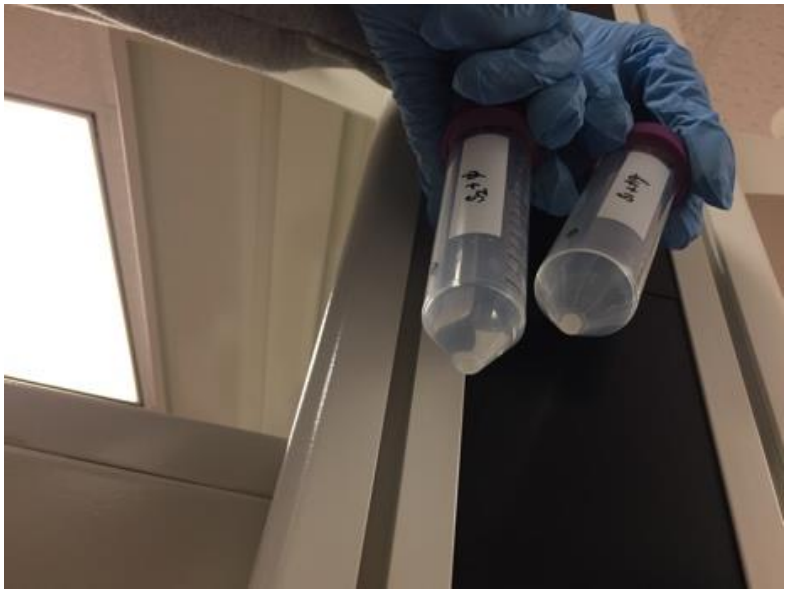

Figure 8. Cell fixation by adding 37% formaldehyde to the cell cultures.

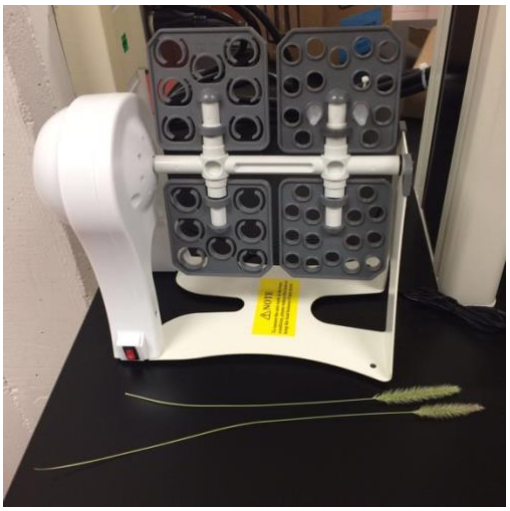

Figure 9. The final sample was stored in 1X PBS solution and placed on the nutator.

2.1.2. Sample Mounting and Imaging

The prepared sample was diluted by five-fold in phosphate-buffered saline. Initially, 3% agarose pads, 5 x 5 mm^2, were prepared. 10 ul of the diluted sample was added to the agarose pad. The sample was incubated at room temperature for 15-30 min until the bacterial cells were absorbed into the agarose pads (see Figure 10). The agarose pad was flipped and attached to the clean coverslip. The chamber was constructed by sandwiching the pad between the coverslip and a microscope slide (see Figure 11). The chamber was sealed using epoxy glue and incubated

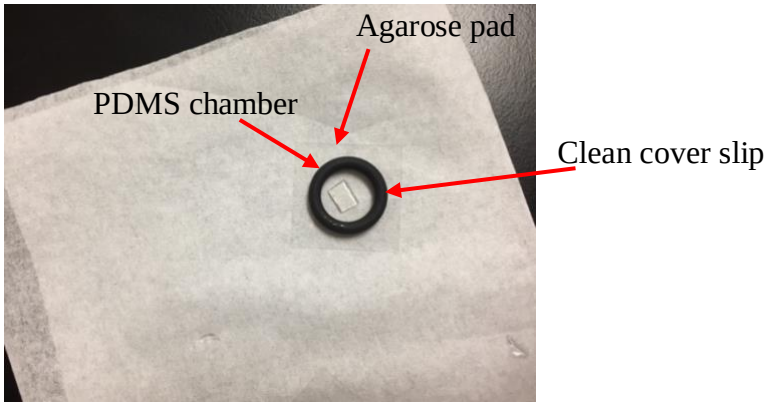

Figure 10. Steps of sample preparation for imaging.

at room temperature for another 10 min in the dark before imaging. This helped prevent water evaporation and shrinkage of the agarose pad during data acquisition.

The microscope was built on an Olympus IX-81 inverted microscope with an Olympus TIRF 60XN.A.=1.49 oil immersion objective [52]. The microscope and data acquisition were controlled by Micro-Manager software [52]. A 405 nm laser (Coherent, CA) and a 532 nm laser

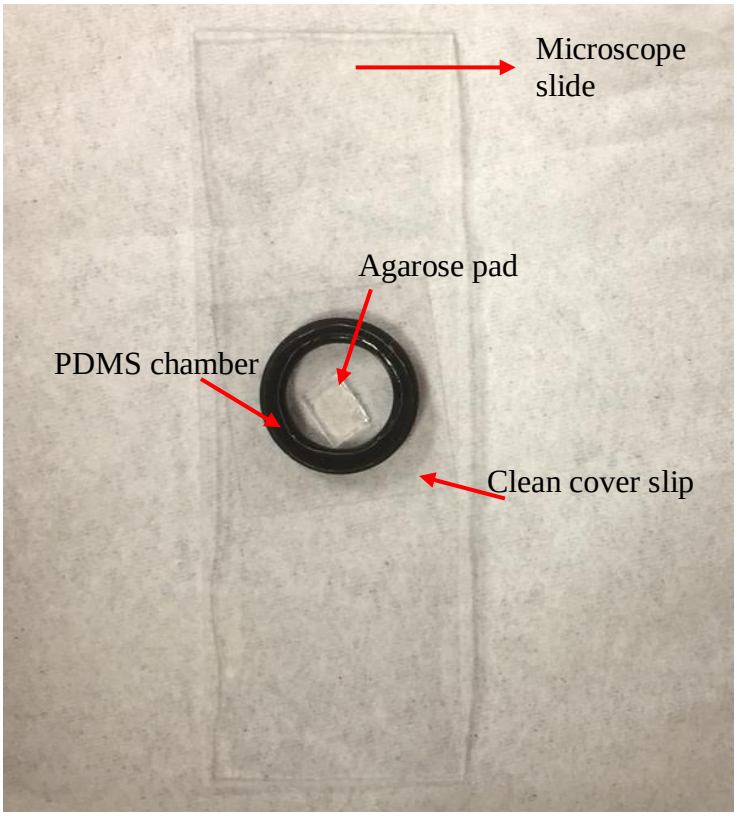

Figure 11. Agarose pad flipped and attached to the clean coverslip.

(CrystaLaser, NV) were used to "activate" and excite mEos3.2-HNS fusion proteins in bacteria. Emissions from the fluorescent proteins were collected by the objective and imaged on an EMCCD camera (Andor, MA). Before the camera, a TIRF lens was inserted so that the total magnification reached 240X. The sketch of the microscope is shown in Figure 12. 405 nm and 532nm lasers are used to excite the fluorophores. Shutters and ND filters were placed in front of

the lasers. The operation of the lasers was as follows: when the lasers were switched on, lasers reflected off the mirrors, and both the 405 nm and 532 nm lasers met near the dichroic mirror. These lasers together passed through the dichroic mirror, and reflected off the last mirror. Then, they passed through the beam expander, TIRF lens, entered the Olympus IX 73 microscope, and passed through EMCCD camera. Finally, the data was collected in a computer connected to EMCCD camera.

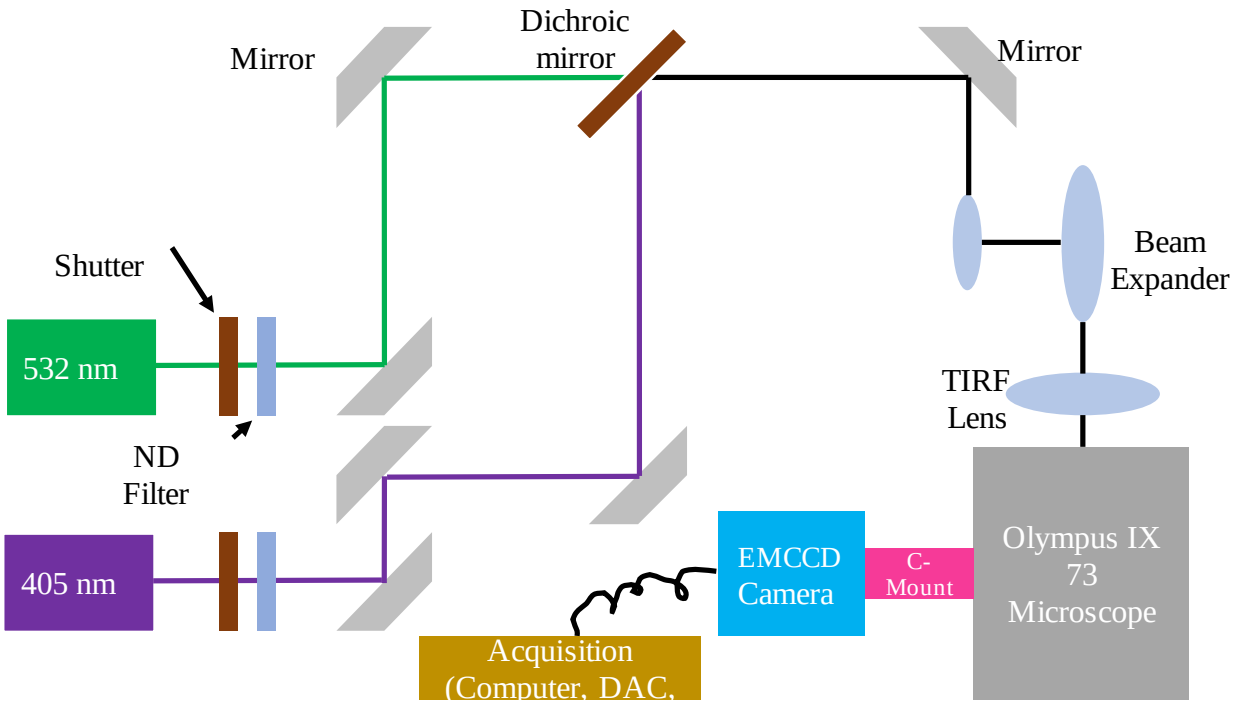

Figure 12. Setup of super resolution microscope.

The resulting movies (20,000 frames) were analyzed using rapidStorm software [53]. The localizations that were present in adjacent frames and within 10 nm to each other were considered as a single molecule. The spots that were blurry, broad, or narrow, were discarded. The remaining spots were further drift-corrected using a mean cross-correlation algorithm and were used for developing super-resolved images for further quantitative analysis (see Figure 13).

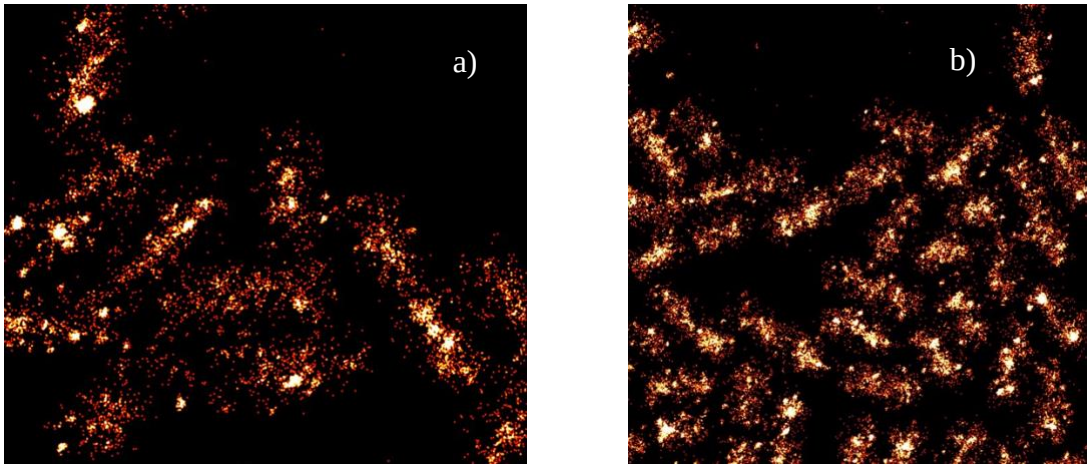

Figure 13. Super resolved images of H-NS proteins a) in the presence of silver ions and b) without silver ions.

2.2. Data Acquisition

2.2.1. Micro-Manager Software for Controlling Super Resolution Microscopy

For many years, managing optical microscopes was a tough job, which involved the usage of many hardware modules. Originally, the pictures were saved by hand drawings and later the pictures were saved on film [54]. Now, with the advancements of microscopes, their features can be controlled by computer software. The advancements in microscope modules significantly increased simplicity and have increased the opportunities in many research areas [54]. The advancements in microscopes enable some features to be controlled automatically. Examples include: the control of color, contrast, intensity, filter wheels, duration of the light exposure on the mounted sample, etc. The digital microscopes allow the user to capture enormous images or videos with accurate pixel sizes and the images or videos can be stored and analyzed depending upon the requirement [54]. To perform all these actions, software is needed which can control all the actions of the microscope. As the demand for powerful microscopes is increasing, the demand for microscope controlling software in the field of microscope research is

also increasing. Several software packages are available for controlling microscopes. For instance, some of the software include: LabView, MetaMorph for molecular imaging, Olympus SlideBook, Nikon NIS Elements, Openlab, and Zeiss Axio Vision [54].

Since 2005, associates of Ron Vale's laboratory in University of California San Francisco (UCSF), along with other sponsors, have been developing a free open-source software, Micro-Manager, which has the capability of controlling all systematized microscopes, cameras, and other peripheral equipment from different manufacturers and is compatible with Windows, Mac, and Linux computer-based systems [54]. Micro-Manager is user-friendly and can be used with the Windows based graphical user interface (GUI) for normal and advanced microscopes [54]. Micro-Manager can also be used or synchronized with Image J software, which is a free and open source software for the analysis of images and is used by many biologists [54]. Micro-Manager has provisions for various mechanical microscopes such as Nikon, Olympus, Zeiss, Leica; cameras such as Andor, Stanford Photonics, Photometrics, PCO, IIDC Firewire; stages such as ASI, Physik Instrument, Mad City, filter wheels, data acquisition boards, illuminators (Cobolt, CoolLED, Conix, Sutter, Thorlabs, Nikon), data acquisition and other accessories [54]. Micro-Manager software makes microscopes move user-friendly to non-expert users [54]. Micro-Manager software is self-explanatory and users who access the software can handle or control any microscope, camera, or stage.

To capture an image using a microscope, the user performs a sequence of steps. To image a sample, the basic steps involved are: changing the color of the filter wheel, changing the intensity of the laser, adjusting the sample slide, adjusting the focusing position, finding the right exposure time, opening the shutter of the microscope to start imaging, changing the camera exposure time, and capturing and storing images. These activities can be carried out smoothly and can be executed frequently with the help of Micro-Manager software.

Protocol for using the Micro-Manager software:

The Micro-Manager software was downloaded from the website [54] [55]. Follow the instructions given to install the software for the operating systems such as Windows, Mac or Linux. After the installation of the software, startup of Micro-Manager will also start Image J. Micro-Manager and Image J windows appear differently on the screen of the computer. The Image J window helps in the analysis of the images. Micro-Manager displays a pop-up screen that allows one to choose a hardware configuration file. If you click "OK" without changing anything, the last successfully used configuration file will be loaded [54]. It also has a drop-down menu, which lets users select a configuration file [54]. Once the configuration file is set up, the camera clicks, indicating that the camera is on and the Micro-Manager main window appears. The main window of Micro Manager typically has two parts. The top half part is used to control the microscope and manage the settings as per the requirement. It consists of a series of column and row icons.

The [Snap] button allows the capturing of a single image from the camera, which can be edited and saved by using the Image J tool [54]. The [Live] button allows taking images in the live mode and the captured images are saved directly. The "Acquire" icon allows taking the images. By clicking on the [Multi-D Acq] button, it allows opening the multi-dimensional acquisition window where the number of the frames can be given as input needed for a picture. The values of several frames can be varied. The [Burst] button allows taking images with high speed. Next is the row of icons. The [ROI] (Region of Interest) button is used to configure only the region that is needed for collecting the data. The [Zoom in] and [Zoom out] buttons are straightforward. The top left part contains the camera settings where one can control the exposure time, binning (grouping the pixels of the camera), shutter, and auto shutter options [54]. The bottom part of the window generates the histogram of the captured image and helps in

adjusting the brightness and contrast of the images as needed. The Micro-Manager window is shown in Figure 14.

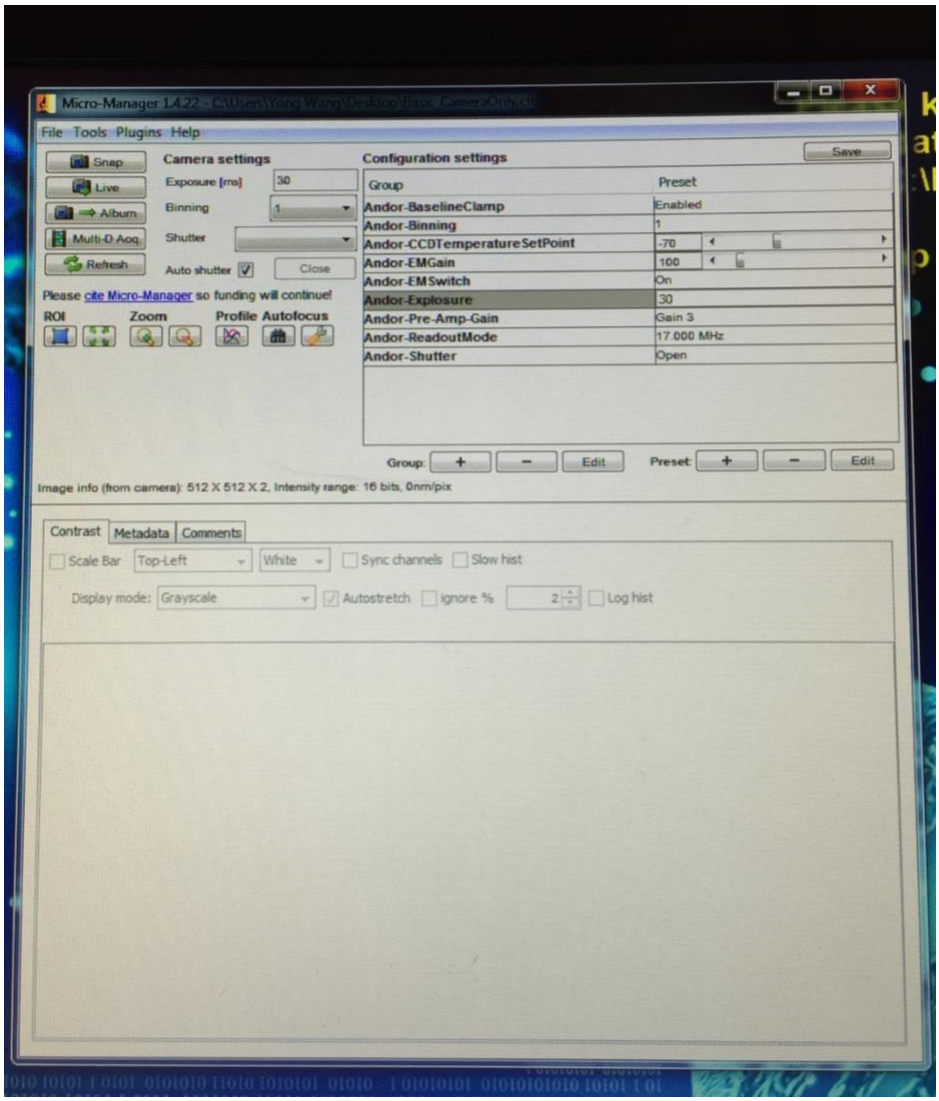

Figure 14. The Micro-Manager main window used for acquiring super resolution microscopy data.

2.2.2. Imaging the Sample Using Micro-Manager

Following is the procedure for imaging the sample using Micro-Manager. Open the Micro-Manager software and configure the files and press the [ok] button. Once this is done, a click sound can be heard from the camera and the main window opens. Click on the [live]

button on the main window and make sure not to exceed 5 s to close the live window. Meanwhile, mount the sample by adding a drop of oil on the objective lens. Open the shutter and switch on the laser. The configuration settings on the Micro-Manager are changed. The EM Gain is set to 100; the exposure time is set to 30 ms. Click on the live icon and select the region of interest by pressing on the [ROI] button. Select the multi-dimensional acquisition window, and input the number of frames. During the experiment, 20,000 to 50,000 frames are typically acquired for an image. Specify the file name and press the [acquire] button. The acquired image or the video is stored in the form of tiff files in the specified location.

2.2.3. rapidSTORM Software for Super Resolution Microscopy

Over the years, there has been an intense development in the usage of super resolution microscopy, which is super resolution fluorescence imaging using photoactivation, photo switching, or any other fluorescence generating process [53]. To access the microscopy, an open source, quick, and very potent software named ‘rapid accurate program implementing direct stochastic optical reconstruction microscopy (rapid STORM) is available [53]. rapidSTORM software is extensively used for localization microscopy and has 60,000 lines of code with less replication and is mostly used in the academic field [53]. rapidSTORM is the only public software which can use, or provide provisions for, several different microscopes such as classic localization microscopy, multicolor localization microscopy, and 3D multiplane astigmatic microscopy [53].

In the rapidSTORM software, the given input data is managed sequentially; maximum spots are found in the input image and are fitted with the Gaussian PSF model with the help of the Levenberg-Marquard fitting routine [53]. For localization, rapidSTORM uses the Levenberg-Marquard fitting either with the help of least-squares metrics or with Poissonian MLE

distance metrics [53]. When compared with open source software for super resolution microscopes such as QuickPALM1.1, Palm3D0.1.6, M^2LE3, and Octane1.2, rapidSTORM software has several features that are not accessible in other software [53]. The features of rapidSTORM software compared to QuickPALM1.1software are listed in the Table 4.

Table 4. Comparison of characteristics between open source rapidSTORM 2.21 and QuickPALM1.1 software for super resolution microscopy [53].

Characteristic	**rapidSTORM2.2.1**	**QuickPALM1.1**
Graphical user interface	Yes	Yes
Command line interface	Yes	No
Interpretation of Andor SIF files	Yes	No
Interpretation and Writing TIFF files	No	Yes
Input model for 3D PSFs	Yes	No
Least – Squares fitting	Yes	No
MLE fitting	Yes	No
Fitting the Gaussian PSF model	Yes	No
2D processing with well-known PSF	Yes	No
2D fitting with good per-spot PSF width	Yes	Yes
Approximation of PSF from input data	Yes	No
Approximation of 3D PSF from input data	Yes	No
3D by means of astigmatism & biplane	Yes	No
Gaussian 3D theoretical and calibration model curve	Yes	No
Multicolor and Two- kernel analysis	Yes	No
Capability of observing results during the process	Yes	Yes
	Yes	No
Time determined images and movie clips	Yes	No
Able to do Linear drift correction	Yes	No
Ability to track particles	Yes	No

rapid STORM Usage and Settings:

Overall, the rapidSTORM software is user-friendly and straightforward. After opening the rapidSTORM software, the main window pops up. Options are selected to generate the localization file. Initially, from the user level, the Intermediate option is selected and the desired input TIFF file is selected. In the Input layer section, set the input pixel size to 160 nm and set the full width at half maximum of the point spread function in the PSF FWHM field to 300 [53].

The minimum spot distance is set to 3PX, and the Intensity Threshold is set from 1000 to 15,000 [53]. The value is predicted by the type of numerical aperture used for the microscope, by approximating $\lambda/2\mathrm{NA}$ [56]. λ represents the detection wavelength and NA is the numerical aperture of the objective [56].

In the rapidSTORM engine, the following options are selected. The minimum fitted emission intensity is necessary for a spot to be considered a localization. If the fitted position has an intensity lower than this value, it is discarded as an artifact and option [Smooth by Average] in the spot finding method is selected. The [Smoothing mask width] option is set to 5PX and this helps smooth by median and by average. The [Fit window radius] option is set to 600 nm. The [Iteration limit] is set to 100, and by doing so, the nonlinear fit process for the localization attempt is stopped after the given value. The PSF width is a free fit parameter and the [Store PSF width] option is selected. The option [Store PSF width] helps in storing the PSF width information in the localization output files. In the [output file] button, [Display Progress], [Count Localizations], [Localization File] and [Image Display] output options are selected. Finally, the [RUN] button is selected and the output file is saved in the form of a text file.

2.2.4. Cleanup of Data

The next step is to clean up the data from the previous step. The output of the data is a $n \times 8$ array, where n is the number of localizations. Table 5 describes the format of the data in each column.

Table 5. Cleanup data format

Column index	1	2	3	4	5	6	7	8
Description	X coordinate	Y coordinate	Frequency	Amplitude	Wx	Wy	Resolution	Bg

For each pixel in the image, the Gaussian smoothing algorithm is used to remove noise from the image. This reduces any unwanted pixel in the TIFF files. The algorithm shown in Figure 15 illustrates the steps followed to clean the data.

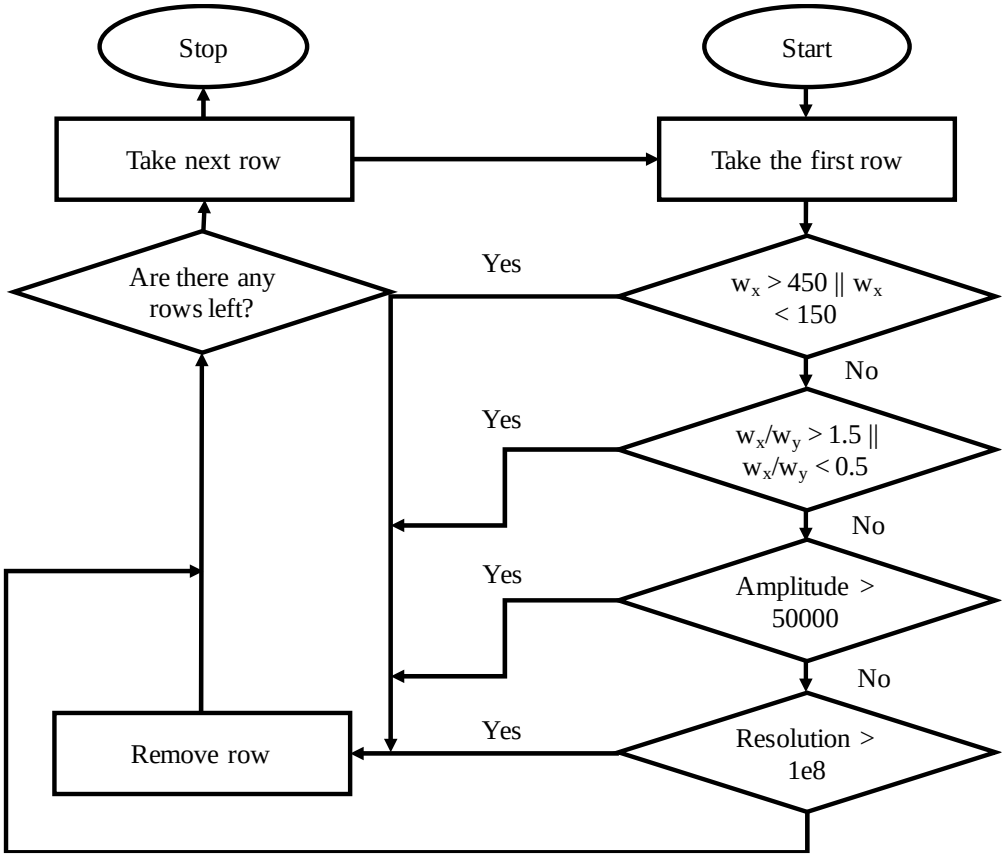

Figure 15. Algorithm illustrating cleanup of data.

2.2.5. Drift Correction

The resolution of images has been improved using the super resolution microscope. The image resolution depends on the fluorophores activation and their positions. Usually, several thousands of images are required to restructure a super resolution image. Hence, the super resolution microscope requires longer acquisition time — from a limited time to several hours [57]. The sample always moves after a while during the acquisition causing drift. To attain higher resolution in the images, drift correction is crucial between the microscope and the

imaging optics, i.e., the objective lens used for imaging. Drift correction is important for analyzing organelle structures and protein complexes. Drift typically can be corrected either by stabilization during acquisition or correction after acquisition. Post-acquisition drift correction is uncomplicated as there is no need for adjusting the microscope while acquiring images. In both conditions, precise drift correction is essential. The movement of sample causing drift during acquisition can be prevented by hardware clarifications, such as setting the objective lens to the stage or by controlling the position of the sample on the image plane with the help of the control system [58]. Axial drift takes the samples out of focus and it can be corrected in a similar way to lateral drift [58].

A common method for drift correction is using the appropriate fiducial marker (small fluorescent beads) in the sample [57]. The drift is measured by tracking the marker positions. This method is time-consuming and the markers should not be bleached during the time of data acquisition.

Another method is using the mean cross-correlation algorithm, which overcomes these issues. This method is used in the fields of localization events-based cross-correlation. The advantage of using this method is there is no need for the adjustment of the microscope and the time required for acquisition. In this method, the drift correction accuracy is up to the 5 nm level [57]. The algorithm used for drift correction is shown in Figure 16.

The localizations which were within 10 nm frames and were neighboring to each other were considered as a single molecule. The spots that were too dim, too narrow or too wide were excluded. The spots that passed these criteria were additionally drift corrected using the mean cross-correlation method. The drift correction program was written in MATLAB.

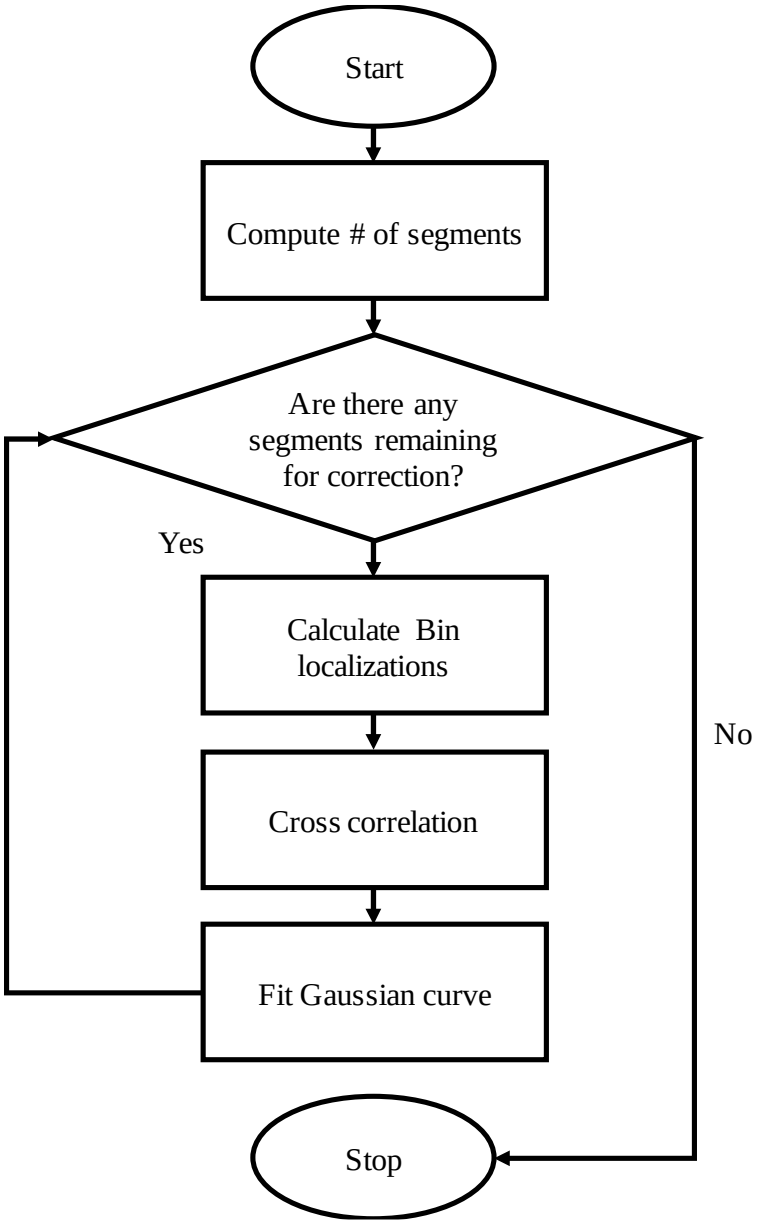

Figure 16. Algorithm for drift correction in the sample collected [57].

Generation of Super Resolution Images:

The saved text file was opened and the first two rows of the text file which contained information specifying each row's details were deleted. To get the render localization image, the written MATLAB code was used, and the text file generated using rapidSTORM was loaded into the MATLAB file. After running the cleanup and drift correction MATLAB script, the final

super-resolved image was generated using Image J software. Using Image J, the saved rendered image file brightness and contrast were adjusted. The image was then rotated 90 degrees and flipped horizontally. The image was scaled exactly to the AVE image. The color of the image was changed by selecting the [LUT] option (lookup table) and Red Hot color was chosen and the image was saved as a PNG file. The original TIFF file was scaled using ImageJ and was saved as PNG file. Finally, the color of the AVE image was changed to green or any other color of preference and the two images, PNG and AVE, were merged to generate the final super-resolved image. The bright field image and the super-resolved images of *E. coli* bacteria are shown in Figure 17.

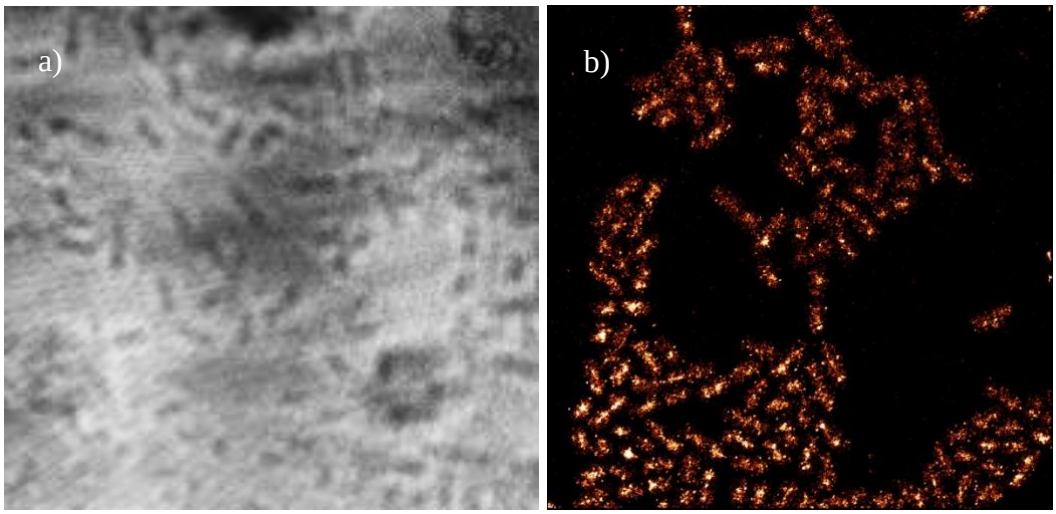

Figure 17. *E. coli* bacteria: a) bright field image b) super resolved image.

2.3. Implementation of Voronoi analysis

Voronoi tessellation is a method of dividing space into convex polygons or regions based on the criteria distance to specific points [59]. These specific points are called seeds. These localizations, received after drift correction, are used as seeds for Voronoi analysis. The regions formed by Voronoi tessellation are called Voronoi cells. Any point in a Voronoi cell is nearer to

the region's seed than to any other seed in the Voronoi diagram [59]. Edges of a Voronoi cell are nothing but a perpendicular bisector of seeds in a Voronoi diagram. Voronoi analysis was performed on H-NS proteins and the Voronoi diagram for the H-NS protein is shown in Figure 18.

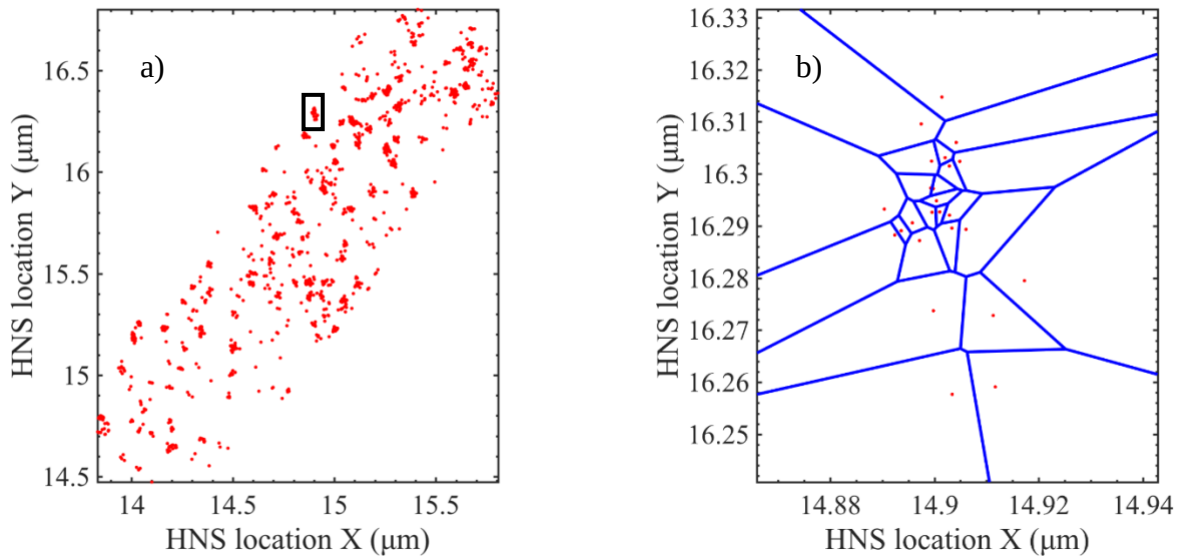

Figure 18. Illustration of Voronoi analysis. a) H-NS localizations before Voronoi analysis. b) Voronoi analysis of a small region enclosed by black rectangle in (a).

For the experiment, a Voronoi diagram was used to perform special analyses of H-NS proteins. To perform this analysis, the Voronoi tessellation method was used. In MATLAB, Voronoi tessellation can be performed by using a predefined function

$$[V, C] = \text{Voronoi}(A) \qquad \text{(Equation 8)}$$

This equation gives information about Voronoi vertices and Voronoi cells which are V and C of the Voronoi diagram of A. V indicates the *n*-by-2 array of the *n* Voronoi vertices in two-dimensional space; each row represents x coordinate and y coordinate of a Voronoi vertex [60]. C is a vector cell array, where each element gives the information of the indices into V of

the vertices of the corresponding Voronoi cell [60]. A is nothing but a seed array [60]. A seed array contains two columns. The first column represents the x coordinate of the seeds and the second column indicates the y coordinate of the seeds.

Once V and C are calculated, adjacent seeds in the Voronoi diagram are identified. This helps in calculating quantitative parameters. A seed is considered adjacent to another seed if both share a common ridge. This can be identified using output from Voronoi tessellation. C, that provides indices to Voronoi vertices, can be used for this purpose. The first vector array in C is the collection of indices to vertices around the first Voronoi seed in A. By performing a pairwise look up in each vector array of C, ridges and vertices that form those ridges were identified. This adjacency information is used as input for further calculations of quantitative parameters.

2.3.1. Quantitative Parameters

Area, density, and mean distance of Voronoi cells at the k^{th} rank were calculated to analyze the spatial orientation of the localizations. Area is nothing but the amount of space occupied by a Voronoi cell in two-dimensional space. To calculate the area of a cell, a MATLAB method called *polyarea* was used. This method takes an array of points as input parameters. Voronoi vertices of the seed were passed as input parameters to calculate the area. This step was repeated for every localization of drift-corrected data. The next step was to calculate area, density, and mean distance at k^{th} rank. Rank denotes how far a Voronoi cell is located from a given cell. For any given cell, Voronoi cells at 1^{st} rank are all immediate neighbors of the cell. Voronoi cells at 2^{nd} rank are all immediate neighbors of immediate neighbors. That means, Voronoi cells at 2^{nd} rank are two cells away from the current cell. Similarly, Voronoi cells at k^{th} rank are k cells away from the current cell.

Definition for Parameters:

Area at k[th] rank A_i^k= Sum of areas of all cells till k[th] rank [59].

Density at k[th] rank δ_i^k = Number of Voronoi cells till k[th] tank ÷ Area at k[th] rank [59]

Mean distance at k[th] rank d_i^k= mean of the Euclidean distances between all the seeds of Voronoi cells at k[th] rank [59].

The area of a Voronoi cell at k[th] rank is illustrated in the Figure 19. Let A_i be one of the seeds in given localizations. All Voronoi cells at 1[st] rank ($k=1$) from A_i are denoted in amber color. All Voronoi cells at 2[nd] rank ($k=2$) are denoted in blue color. The mean distance of a Voronoi cell at k[th] rank is illustrated in Figure 20.

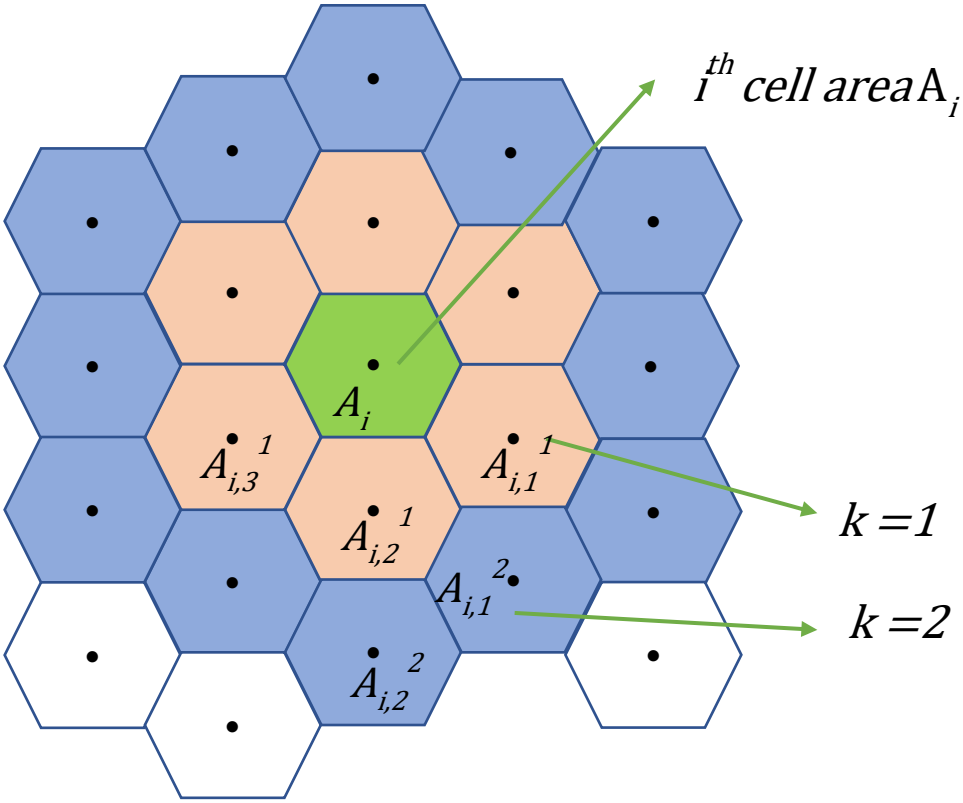

Figure 19. Illustration of area of a Voronoi cell at kth rank.

To validate that the algorithm worked as expected, the algorithm was used against a

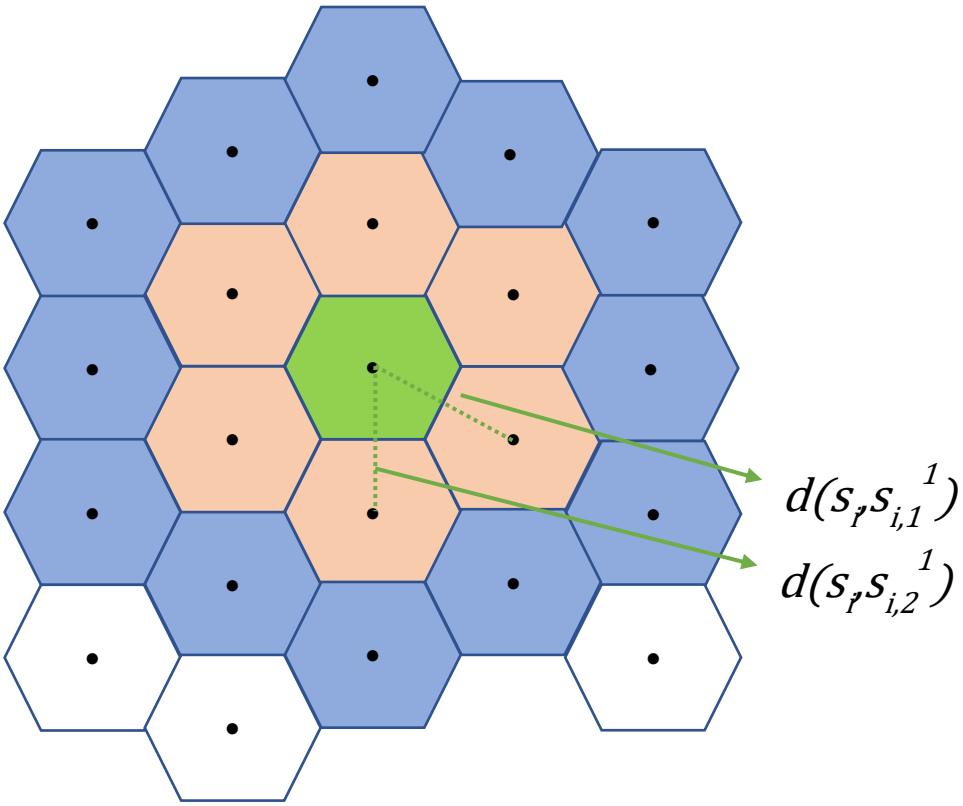

Figure 20. Illustration of mean distance of Voronoi cell at kth rank.

square lattice as shown in Figure 21a and a hex lattice as shown in Figure 22a. Results of this experiment confirmed the accuracy of the algorithm.

In Figure 21a, area of the cells at the edge of the Voronoi diagram are considered infinite. Since localizations of Voronoi cells that are at the boundaries of a Voronoi diagram do not have an enclosed area, the area of the Voronoi cell is considered infinite. All localizations from (1,1) to (1,10) have infinite area. Localizations at coordinates (2,2), (2,9), (9,2) and (9,9) have an area of 3 square units at 1st rank. All localizations with coordinates (3,2), (4,2), … (8,2) have an area of 4 square units at 1st rank. Similarly, all Voronoi cells from (3,3) to (8,8) have an area of 5 square units at 1st rank.

This can be observed in Figure 21b. There are 4 cells with area 3 square units (corner cells), 24 cells (6 cells each on top, bottom, left, right of the lattice) with area 4 square units, and

36 cells (remaining cells in the middle) with area 5 square units. The density of Voronoi cell at 1st rank in the square lattice is shown in Figure 21c. Since all Voronoi cells are of unit square area and localizations are equidistant from one another, the square lattice has uniform density and uniform mean distance (see Figure 21d).

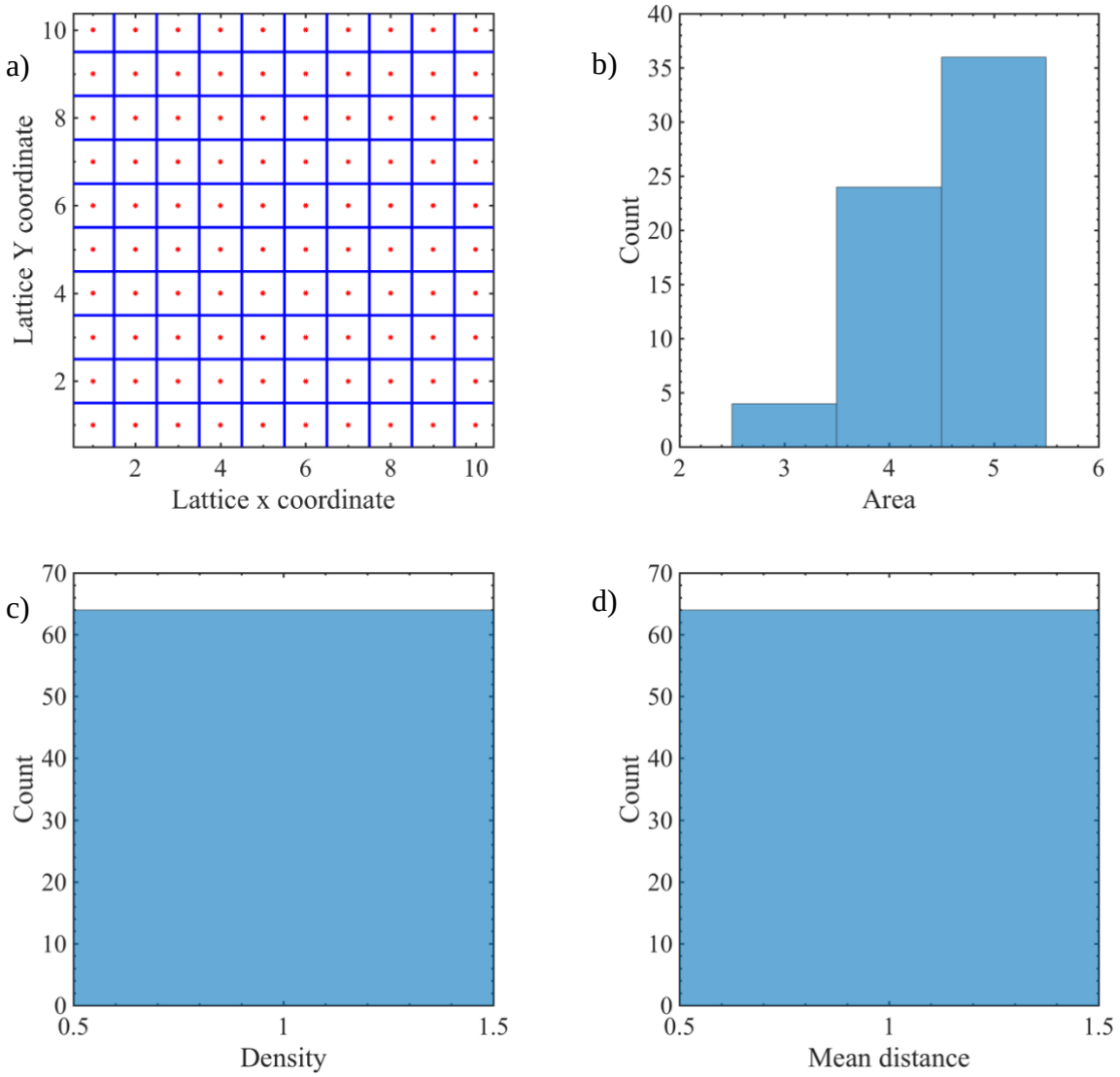

Figure 21. Illustration of square lattice. a) Red stars denote localizations. Blue lines denote perpendicular bisectors of the localizations. b) Area of Voronoi cells at 1st rank in a square lattice. c) Density of Voronoi cells at 1st rank in square lattice. Since all Voronoi cells are of unit square area and localizations are equidistant from one another, the square lattice has uniform density. d) Mean distance of Voronoi cells at 1st rank in square lattice.

To further prove the accuracy of the algorithms, Voronoi tessellation was performed on a hex lattice (shown in Figure 22) and quantitative parameters were again calculated. Uniform mean distance confirms the accuracy of the algorithm.

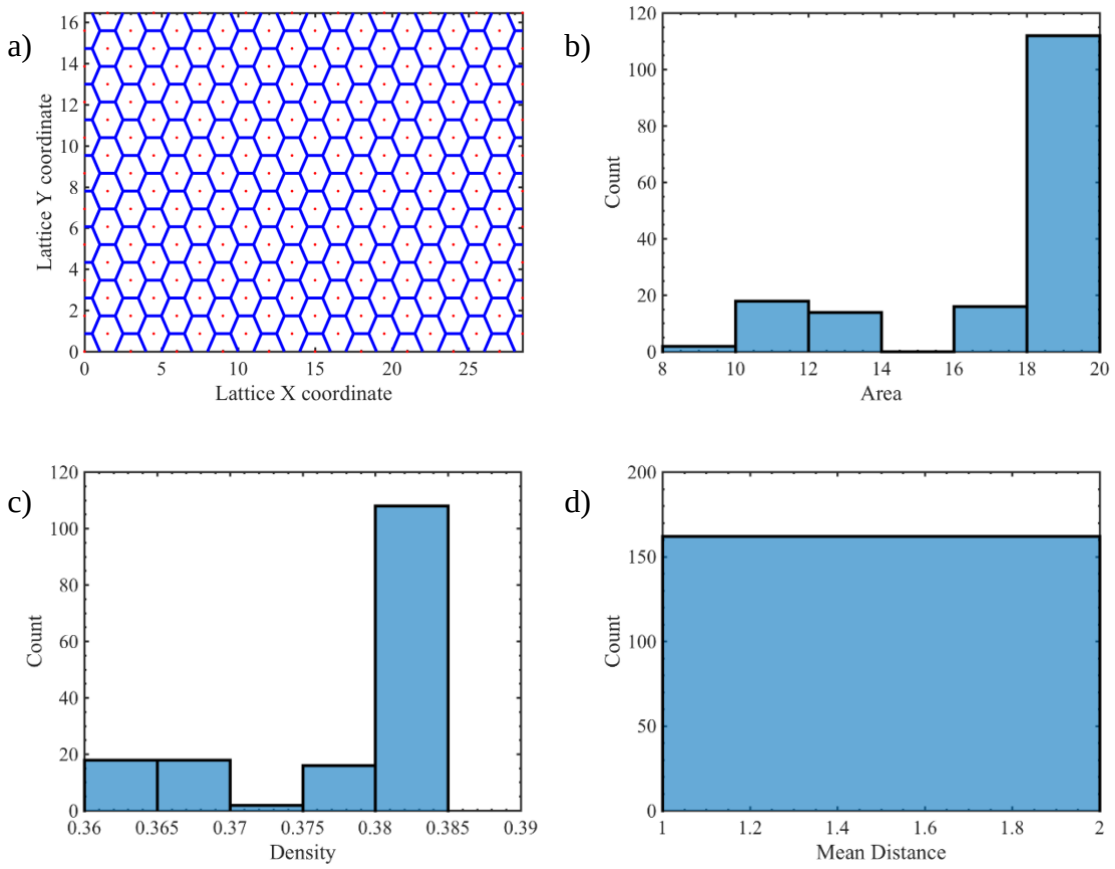

Figure 22. Voronoi tessellation of hex lattice. a) Red dots denote localizations or seeds. Blue ridges are perpendicular bisectors of localizations. The point where these bisectors meet are Voronoi vertices. b) Histogram depicting the areas of Voronoi cells in a hex lattice. c) Histogram depicting the density of Voronoi cells in a hex lattice. d) Histogram depicting the mean distance of Voronoi cells in a hex lattice.

2.3.2. Identifying Clusters in a Sample

Once all the quantitative parameters were calculated, clusters were identified in a sample to determine if silver ions impact cluster formation or not. Clusters are nothing but four or more

localizations grouped together as shown in Figure 23. The grouping logic used was the density of each Voronoi cell where a localization was present. An algorithm that identifies clusters based

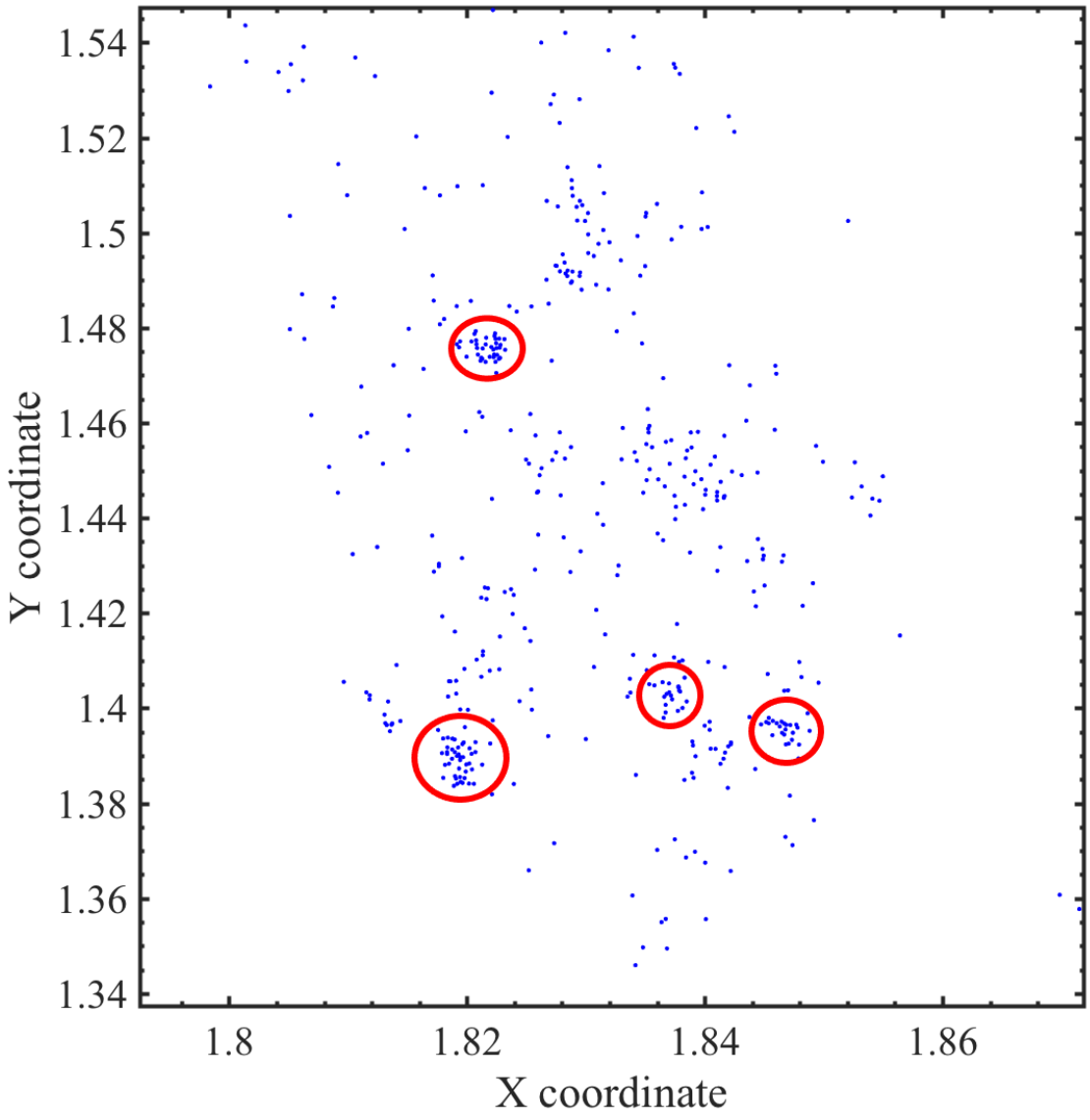

Figure 23. Clusters in a sample. Blue dots denote localizations. Red circles denote clusters where three are more localizations are placed spacially close to each other.

on density of each Voronoi cell at k^{th} rank was written using a recursion method.

A localization is considered part of a cluster if the density of the Voronoi cell is more than twice the average density of the sample. Pseudocode to identify clusters of a sample is shown below. A localization is considered part of a cluster if the density of the Voronoi cell containing the localization is more than twice the average density of the sample. The method GetClusterInfo() calls itself for each immediate neighbor of i until there are no immediate neighbors with density more than the threshold density. This process was repeated for each localization that was not a part of a cluster.

```
for each localization i in X do
        if δi > 2δ then
                increment cluster count.  c=c+1
                C = GetClusterInfo (i, X, C)
        end if
end for

GetClusterInfo (i, X, C)
        if i is not part of cluster then
                if δi > 2δ then
                        add i to the cluster C
                for each neighbor of i, k does
                        GetClusterInfo (k, X, C)
                end for
        else
                i is noise and not part of a cluster.
        end if
end if
```

Let s_i be a localization in a sample S, $i \epsilon N$ where N is the number of localizations. δ_i is the density of localization s_i at k^{th} rank [59], then threshold density of the sample can be calculated as show in the Equation 11.

$$\delta = \frac{\sum_i^N \delta_i^k}{N} \qquad \text{(Equation 11)}$$

All seeds in square lattice are equally placed. Average density of the lattice is same as that of the density of each Voronoi cell formed by Voronoi tessellation. $\delta = \delta_i$ for every value

of i where i ϵ N. To assess the validity and accuracy of the algorithm, this algorithm was employed on a square lattice where there were no clusters.

As illustrated in Figure 24, each Voronoi cell in a square lattice has a unit density and a threshold density of 1 per square unit. Since none of the Voronoi cells has density more than 2 per square unit, one can conclude that a square lattice does not have any clusters.

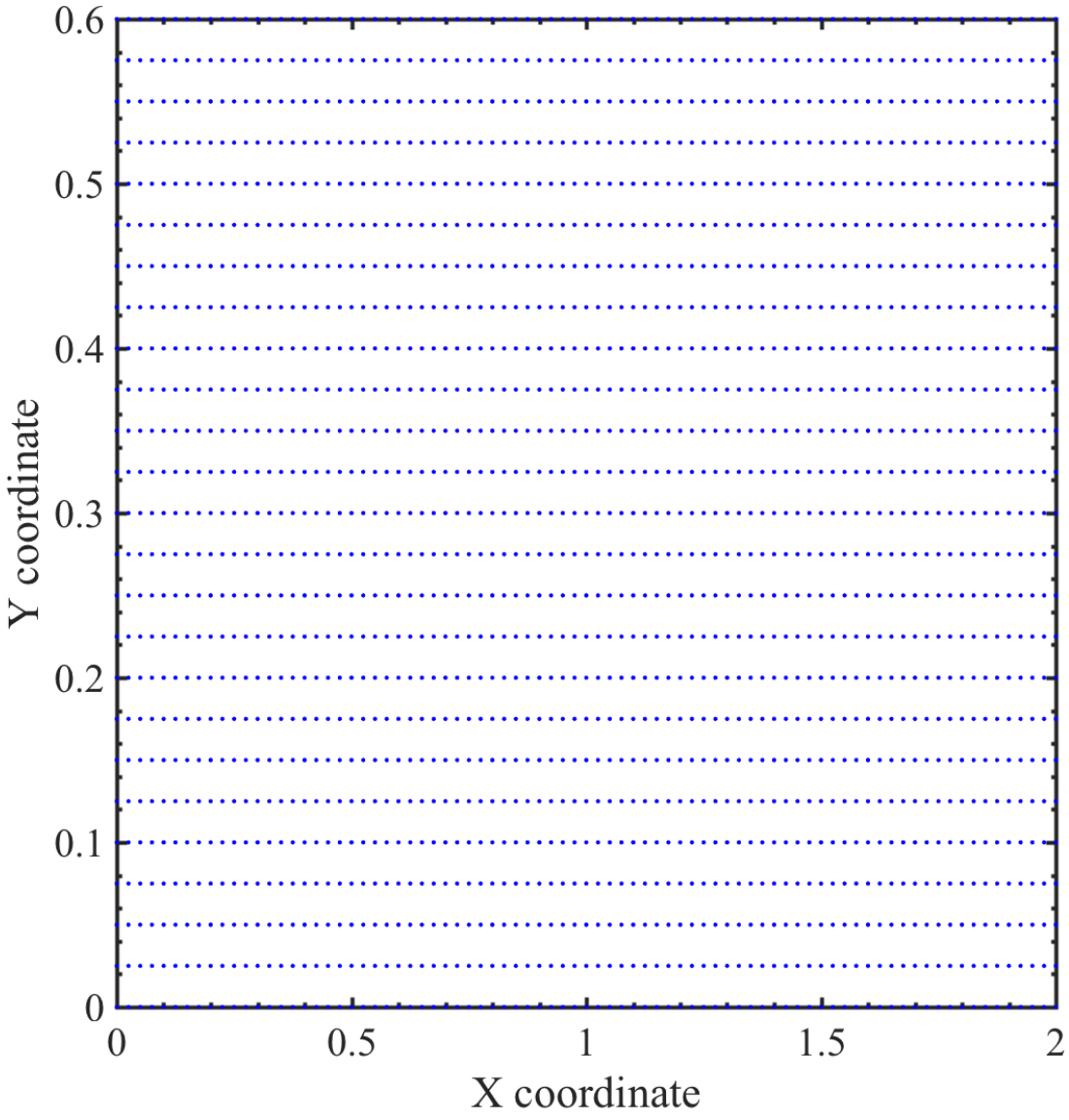

Figure 24. Cluster identification in a square lattice.

Similar verification steps were followed to identify clusters and confirm the accuracy of the algorithm on a square lattice with grid clusters. Grid clusters were placed inside a square lattice at random positions and were given as input to algorithm. This is illustrated in Figure 25.

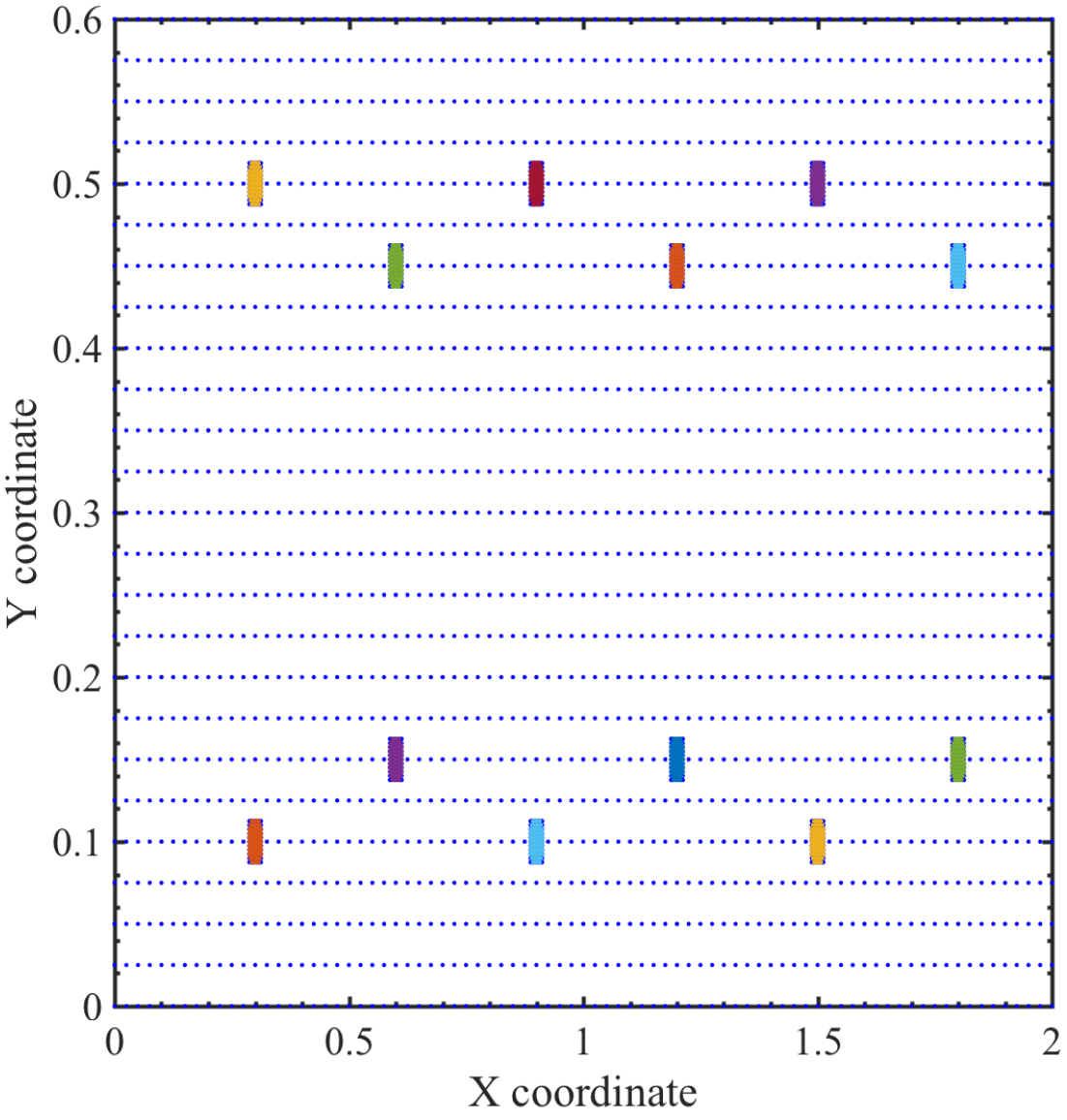

Figure 25. Cluster identification in a square lattice with grid clusters. Blue dots represent localizations or seeds for Voronoi tessellation. Colored regions are groups of localizations that form a cluster in each sample. Each colored region represents one cluster. This sample contains 12 clusters. The density of each localization marked in a color other than blue has a density more than twice the average density of the sample.

Once the algorithm successfully identified clusters in a square lattice, this process was used to identify clusters in random lattice. Figure 26 illustrates the accuracy of the algorithm in identifying grid clusters in a random sample. A random localization lattice was created, and grid clusters were placed within the lattice. This lattice localization data was passed as input parameter to the clustering algorithm.

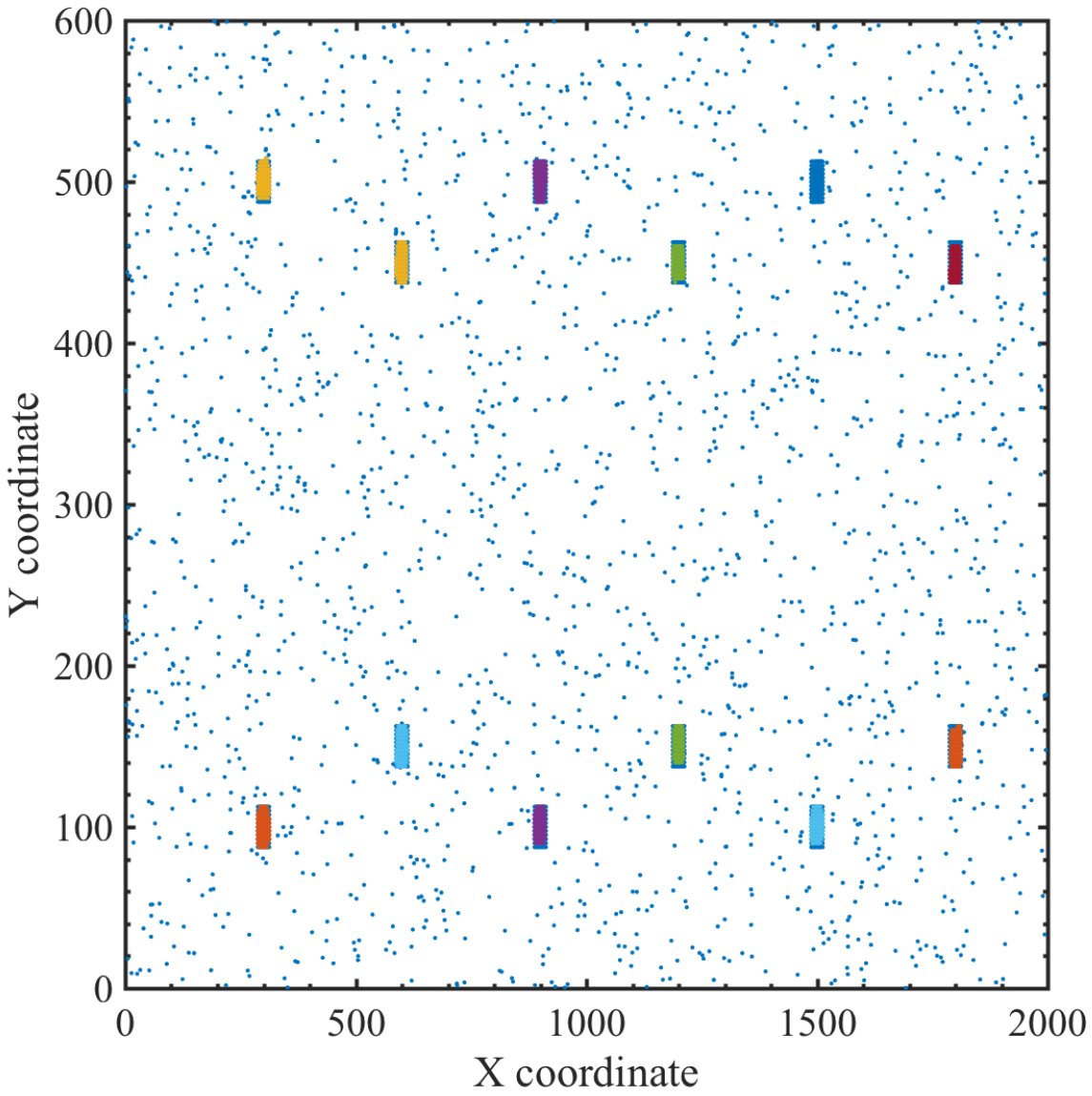

Figure 26. Cluster identification in a random sample. Blue dots show random localizations Colored rectangle regions are grid clusters in the given sample.

This experiment was extended to identify random clusters within a random sample (shown in Figure 27). After confirming the accuracy of the cluster identification algorithm for scenarios described above, the drift-corrected localization data obtained from bacteria cultures were passed as input parameters to identify clusters in the sample. Along with the identification of the cluster, the number of localizations in each cluster, density of the cluster, area of the

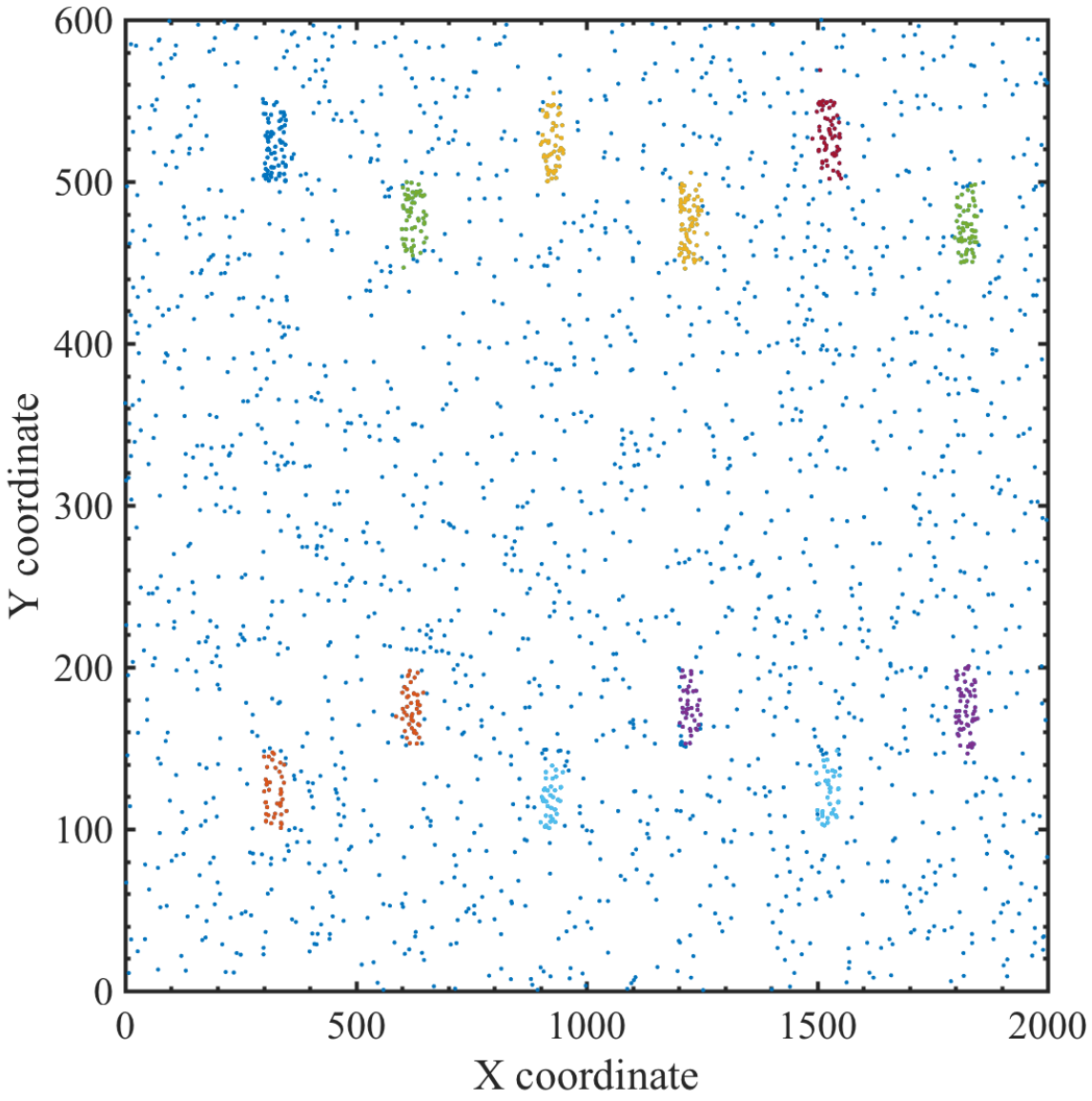

Figure 27. Identification of random clusters in a random sample. Colored dots indicate localizations with density more than that of the average density of the sample.

cluster, and mean distance of the cluster were calculated to get insights to cluster formation in each sample. Localization s_c is considered part of the cluster if it is adjacent to another localization that is part of a cluster and also if the density of s_c is more than the threshold density of the sample.

3. Results

In this chapter, experimental results of H-NS proteins are discussed. Silver ions are known for their anti-microbial properties [2]. Many studies were performed to understand the complete effects of silver ions on the bacteria, *E. coli*. After treating the H-NS proteins with silver, there were many changes in the protein organization in the bacteria cells. The changes were analyzed using clustering algorithms based on density criteria. To illustrate the special change in H-NS localizations with environmental condition, graphs were plotted for the area, density, mean distance, and number of localizations on individual Voronoi cells formed by H-NS proteins and clusters in proteins. Identification of clusters in H-NS protein is shown in Figure 28.

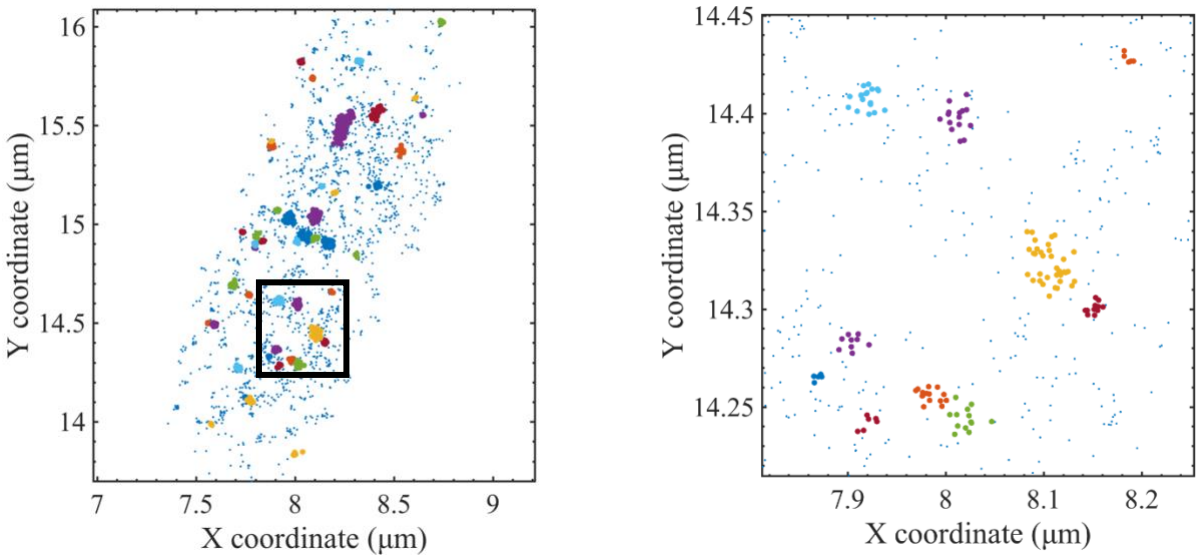

Figure 28. Illustration of clusters in a cell. All localizations have a density of their corresponding Voronoi cells more than twice the average density of the cell. A) Localizations are represented as blue dots. Each colored region is a cluster. B) Zoomed in image of region enclosed by black box in (A).

The clusters in a sample were identified by using the algorithm shown in Figure 29. δ is the average density of the sample. s_i is a seed in the sample. s_j is a seed adjacent to a seed that is

already part of the cluster. Ripley's K-function has been used in the past to study the spatial distribution of H-NS proteins. It was observed that density-based clustering is more accurate and efficient for larger clusters and clusters of uneven sizes [34].

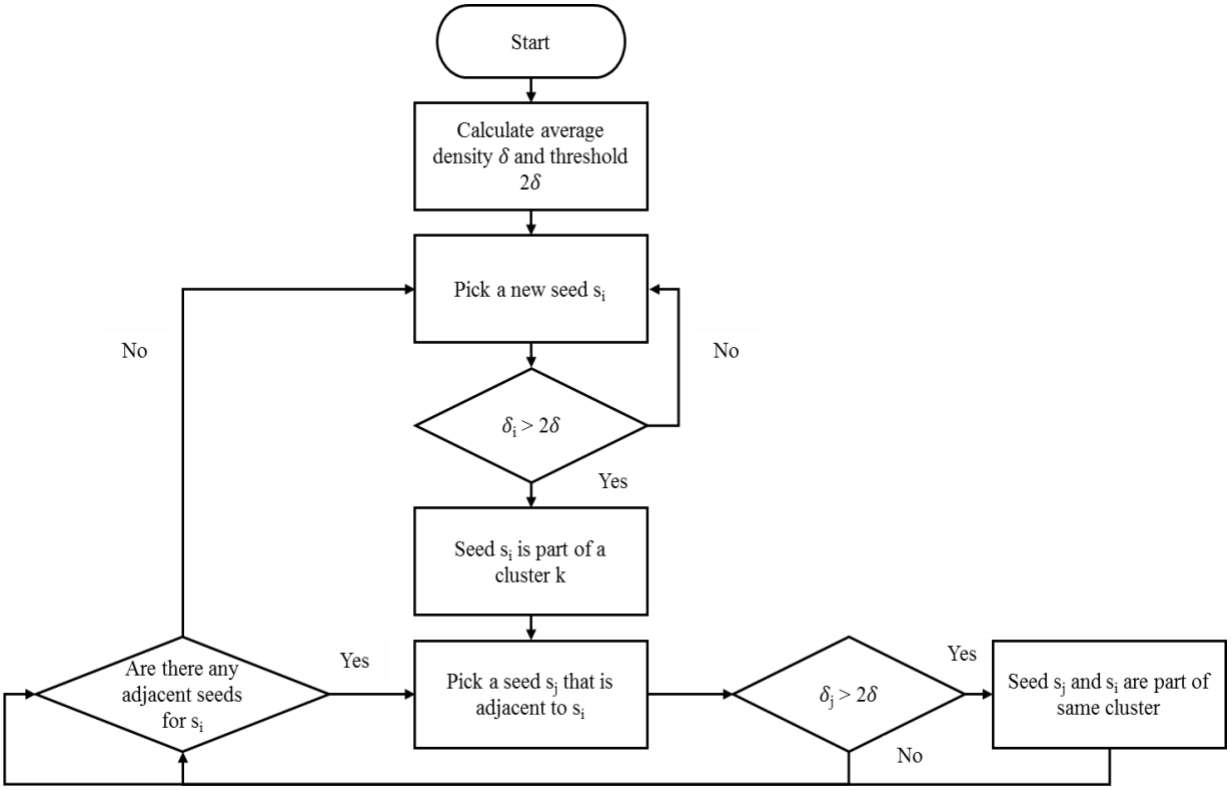

Figure 29. Illustration of algorithm to identify clusters in a sample.

The probability density function of the density of clusters with threshold density being twice the average density of the sample is shown in Figure 30. The red line denotes probability distribution of density of H-NS protein clusters when $AgNO_3$ stock solution was added to the bacteria; the blue line denotes probability distribution of H-NS protein cluster density without silver ions. The probability distribution of cluster density, confirms that probability distribution of density without silver ions is less than that of with silver ions. This could be because of the formation of regions of fewer electrons with the introduction of silver ions [2]. The higher

cluster density of 0.01 nm^{-2} to 0.04 nm^{-2} could be because of an increase in the electron light region and condensed DNA because of the introduction of silver ions [2]. High density can be

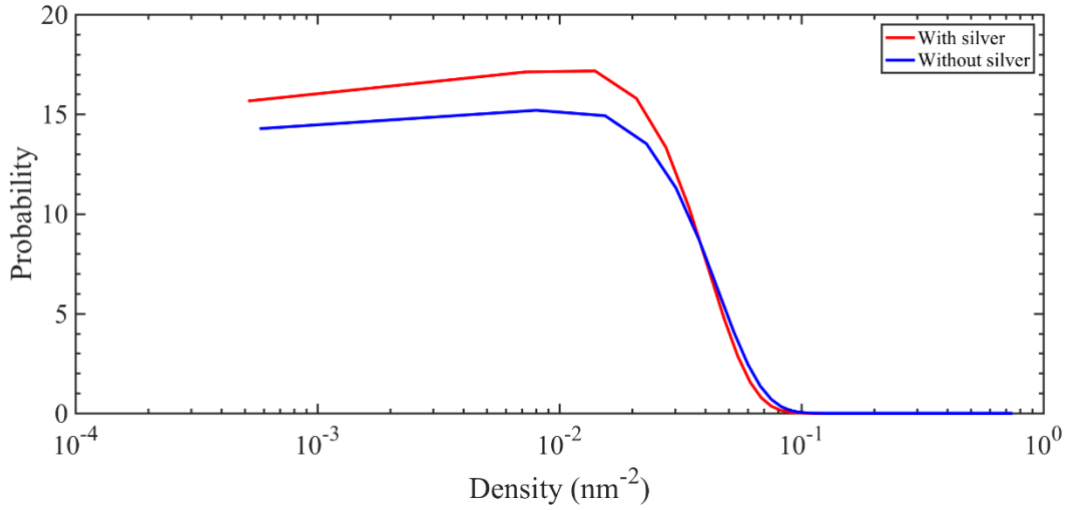

Figure 30. The probability density function of the density of clusters at the threshold density twice that of the average density of the sample.

related to smaller cluster areas of proteins even when the number of localizations were far less when silver ions were present. It can be concluded that these silver ions damage proteins. The formation of denser clusters was less likely when silver ions were added. This can be observed from densities 0.04 nm^{-2} to 0.1 nm^{-2}.

Figure 31 illustrates the probability distribution of the area of clusters with silver ions and without silver ions. Clusters with area more than 10000 nm^2 were observed more without silver ions. This is in line with previous observations that H-NS proteins are spread across the bacteria cell and DNA is at a relaxed state without the presence of any metal ions [2]. The area of a cluster was calculated as the area enclosed by localizations at the boundary of a cluster. The highest probability was observed at an area of 5000 nm^2. For a cluster of area 10000 nm^2 or more, probability was slightly more when sliver ions were not present.

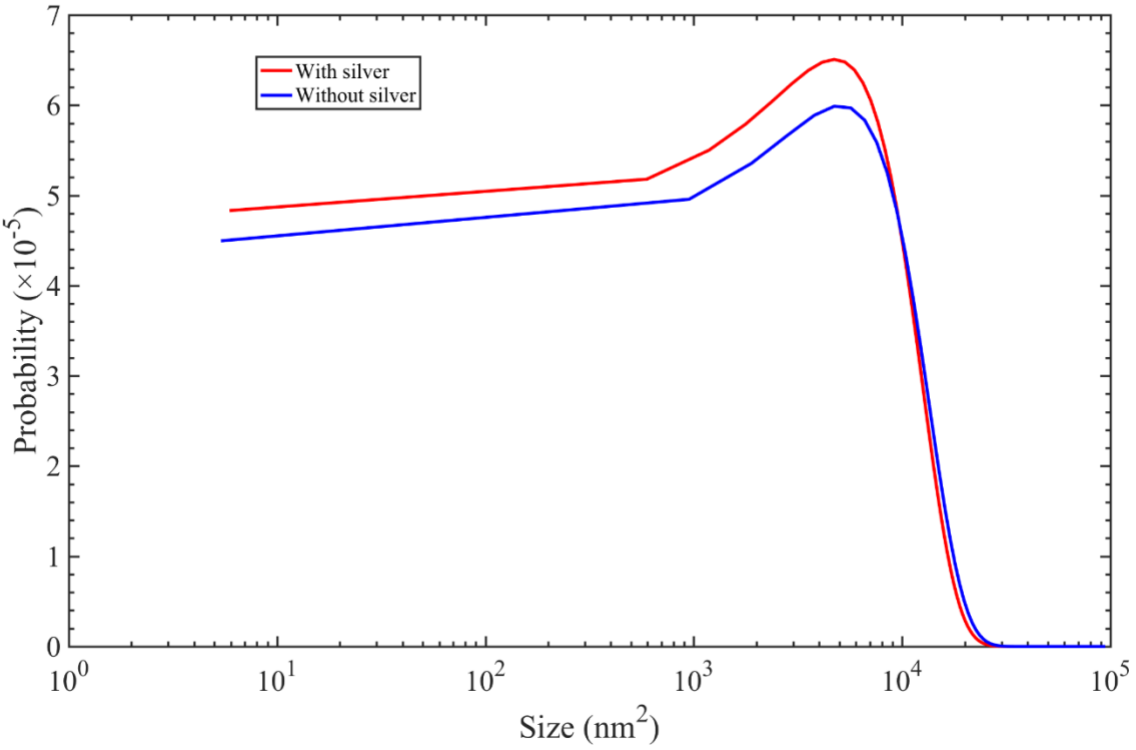

Figure 31. The probability distribution of the area of clusters.

The probability of finding clusters with more localizations was higher when silver ions were not present (Figure 32). This was in-line with the anti-bacterial properties of silver ions. The probability of finding clusters with 40 or more localizations was marginally higher in *E. coli* cultured in silver ions as shown in Figure 32. There were a minimum of three localizations in each of the samples; there are more clusters of 20 localizations or less when silver ions are not present. This is represented as a peak in Figure 32. Low number of localizations per cluster in the presence of silver ions could be because of damage caused by silver ions on *E. Coli*.

The mean distance of localizations in a cluster without silver is slightly more than that of with silver shown in Figure 33. It can be inferred that the condensed DNA because of silver ion's presence is also responsible for small Euclidian distances between localizations. One can conclude that silver ions force H-NS proteins to come together but more research is needed.

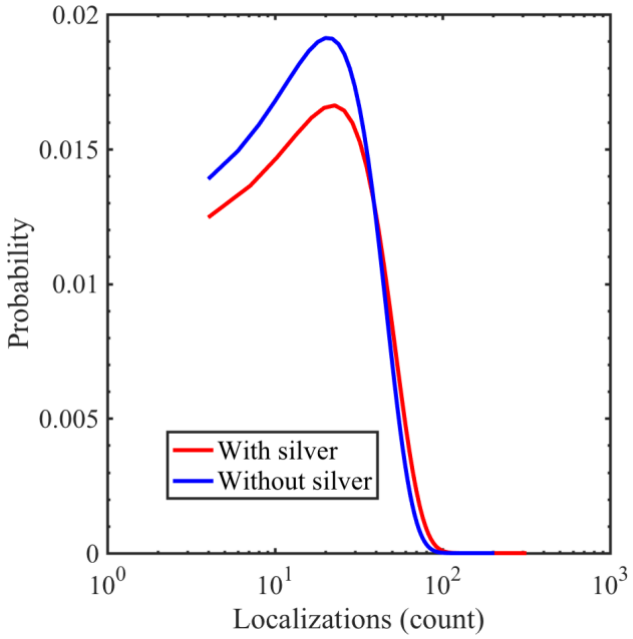

Figure 32. The probability distribution of the number of localizations in a cluster when the threshold density to identify a cluster was twice the average density of the sample. Red line indicates probability distribution when silver ions are present. Blue line indicates probability distribution without silver ions.

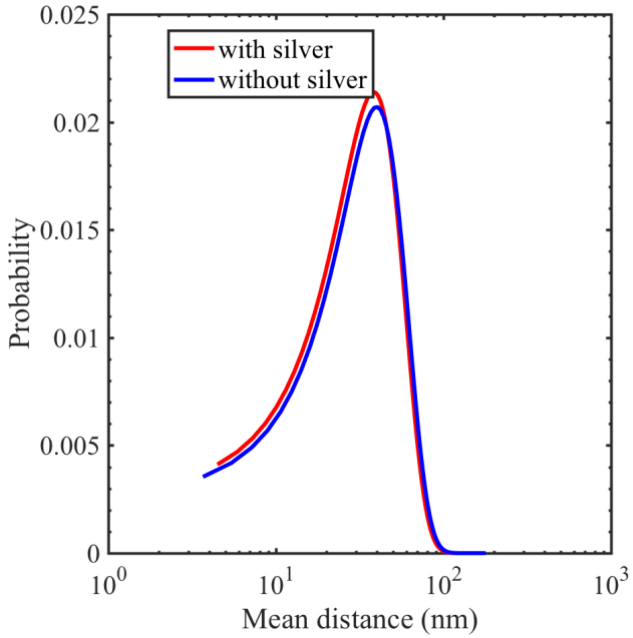

Figure 33. The probability distribution of the Euclidian distance between H-NS proteins in clusters. Localizations are spaced farther apart with Silver ions when compared to that of without silver ions. The minimum distance between H-NS localizations is around 3nm when silver ions are not present. This minimum distance has increased by 1 nm with the presence of silver ions.

4. Summary and Conclusion

In this work, quantitative parameters of H-NS proteins like area, density and mean-distance were computed. A density-based clustering algorithm was developed to identify clusters. For this purpose, average density of the sample was calculated. Any cell with density more than twice the average density of the sample was considered as a localization — forming a cluster. Using super resolution microscopy over conventional light microscopy enabled obtaining high quality images smaller than conventional light diffraction.

Voronoi tessellation method was implemented to investigate distribution of H-NS proteins inside *E. Coli*. Simplicity and robustness of Voronoi analysis make it an obvious choice for analyzing bacterial data. Voronoi tessellation insensitivity to shape of the cell and background noise gave accurate values of quantitative parameters computed. These algorithms were validated against standard square lattice and hex lattice for accuracy. A density based clustering algorithm was also validated against different cluster shapes such as square, rectangle, and random shapes. To acquire the data for Voronoi analysis, H-NS sample was prepared for super resolution imaging. Bacterial strains K12DHNS+HNS-mEos3.2C1were grown in M9GTC medium with antibiotics Kanamycin and Chloramphenicol overnight until the OD600 of the bacteria culture reached 0.2-0.4. The growth medium of the culture was changed by adding silver ions and cell fixation and collection was done. Next, the chamber preparation was done for imaging the sample by using a 3% agarose pad on a clean coverslip and 10 ul of the sample was added to the sample and allowed to incubate for 30 min. The coverslip was sealed using PDMS chamber and the chamber was closed using epoxy glue. The sample was imaged using 405 nm and 532 nm laser. The data was acquired and analyzed using Micro-Manager and rapidStorm. Super resolved images were generated after performing cleanup and drift correction on the acquired data and using ImageJ software.

While experiments conducted on *E.coli* bacteria using silver particles showed the effects of silver ions in changing cell morphological condition [2], the use of super resolution microscopy provided a better understanding of the H-NS protein mechanism inside the bacteria. The formation of H-NS protein clusters inside the bacteria helps explain how bacteria gains resistance to antibiotics. The current Voronoi method is robust even in the presence of noise. The robust nature of the method will have a broad application in the field of single-molecule localization microscopy. Future work must be performed on different microorganisms rather than only on *E. Coli,* to understand whether silver ions are only able to suppress the growth of *E. coli* or it is the mechanism of the bacteria to respond to silver ions.

Finally, even though the current Voronoi analysis and cluster identification helps in identifying clusters in heterogeneous data, more sophisticated algorithms can be developed to identify complex arbitrary clusters in data samples. For instance, it is possible to develop clustering algorithms which would help in identifying complex arbitrary shapes of minerals or fossil fuels present in the environment.

References

[1] A. J. Wesley, "History of the medical use of silver," *Surgical infections*, vol. 10, no. 3, pp. 289-292, 2009.

[2] Q. L. Fend, W. Jian , G. Q. Chen, F. Z. Cui, T. N. Kim and J. O. Kim, "A mechanistic study of the antibacterial effect of silver ions on Escherichia coli and Staphylococcus aureus," *Journal of Biomedical Materials Research,* vol. 52, no. 4, pp. 662-668, 2000.

[3] "Centers for Disease Control and Prevention. CDC twenty four seven. Saving Lives, Protecting People," 6 april 2017. [Online]. Available: https://www.cdc.gov/drugresistance/about.html. [Accessed 10 May 2017].

[4] H. C. Neu, "The crisis in antibiotic resistance," *Science,* vol. 257, no. 5073, pp. 1064-1074, 1992.

[5] X. Li, S. M. Robinson, A. Gupta, K. Saha, Z. Jiang, D. F. Moyano, A. Sahar, M. A. Riley and V. M. Rotello, "Functional gold nanoparticles as potent antimicrobial agents against multi-drug-resistant bacteria," *ACS nano,* vol. 8, no. 10, pp. 10682-10686, 22 September 2014.

[6] H. C. Berg, E. coli in Motion, New York: Springer Science & Business Media, 2008, pp. 11-14.

[7] "Escherichia Coli," [Online]. Available: http://www.redorbit.com/reference/escherichia_coli/. [Accessed 3 July 2017].

[8] G. Reshes, S. Vanounou, I. Fishov and M. Feingold, "Cell shape dynamics in Escherichia coli," *Biophysical Journal,* vol. 94, no. 1, pp. 251–264, 2008.

[9] K. Todar. (2006). Todar's Online textbook of bacteriology. [Online]. Available: textbookofbacteriology.net [Accessed 21 May 2017].

[10] C. J. Dorman, "H-NS: a universal regulator for a dynamic genome," *Nature Reviews Microbiology,* vol. 2, no. 5, pp. 391-400, May 2004.

[11] v. d. Maarel, R. Johan, G. Durgarao, A. Véronique, E. Stefan U., G. Isabelle and F. V. Trevor, "Structure of the H-NS–DNA nucleoprotein complex," *Soft Matter,* vol. 12, no. 15, pp. 3636-3642, 2016.

[12] T. Atlung and H. Ingmer, "H-NS: a modulator of environmentally regulated gene expression," *Molecular Microbiology,* vol. 24, no. 1, pp. 7-17, 1997.

[13] H. Wang, J. C. Ayala, J. A. Benitez and A. J. Silva, "RNA-seq analysis identifies new genes regulated by the histone-like nucleoid structuring protein (H-NS) affecting Vibrio

cholerae virulence, stress response and chemotaxis," *PLoS ONE,* vol. 10, no. 2, p. e0118295, 2015.

[14] R. S. Winardhi, J. Yan and L. J. Kenney, "H-NS regulates gene expression and compacts the nucleoid: insights from single-molecule experiments," *Biophysical Journal,* vol. 109, no. 7, pp. 1321–1329, 2015.

[15] S. C. Dillon and C. J. Dorman, "Bacterial nucleoid-associated proteins, nucleoid structure and gene expression," *Nature Reviews Microbiology,* vol. 8, no. 3, pp. 185-195, 2010.

[16] S. Rimsky, "Structure of the histone-like protein H-NS and its role in regulation and genome superstructure," *Current Opinion in Microbiology,* vol. 7, no. 2, pp. 109-114, 2009.

[17] E. Achtert, C. Böhm and P. Kröger, "DeLi-Clu: boosting robustness, completeness, usability, and efficiency of hierarchical clustering by a closest pair ranking," *Advances in Knowledge Discovery and Data Mining,* pp. 119-128, 2006.

[18] M. Zhang, C. Hao, Z. Yongdeng, Y. Junwei, W. Lijie, J. Wei and C. Juanjuan, "Rational design of true monomeric and bright photoactivatable fluorescent proteins," *Nature Methods,* vol. 9, no. 7, pp. 727-729, 2012.

[19] J. Wiedenmann, S. Ivanchenko, F. Oswald, F. Schmitt, C. Röcker, A. Salih, K.-D. Spindler and G. Ulrich Nienhaus, "EosFP, a fluorescent marker protein with UV-inducible green-to-red fluorescence conversion," *Proceedings of the National Academy of Sciences of the United States of America,* vol. 101, no. 45, pp. 15905-15910, 2004.

[20] A. Yildiz and P. R. Selvin, "Fluorescence imaging with one nanometer accuracy: application to molecular motors," *Accounts of Chemical Research,* vol. 38, no. 7, pp. 574-582, 2005.

[21] Y. Wang, C. En, S. Janet, S. H. Lee, K. W. Teng and P. R. Selvin, "Fluorescence Imaging with One-nanometer Accuracy (FIONA)," *Journal of Visualized Experiments: JoVE,* vol. 91, p. e51774, 2014.

[22] Y. L. Wang and D. L. Taylor, *Methods in cell biology*. Burlington: Elsevier, vol. 30, 1989, pp. 245-270.

[23] J. A. Thorley, J. Pike and J. Z. Rappoport, "Super-Resolution Microscopy: a Comparison of Commercially Available Options," in *Fluorescence Microscopy–Super-Resolution and Other Novel Techniques,* A. Cornea and P. M. Conn, Ed. San Diego: Academics Press, pp. 199-212, 2014.

[24] C. G. Galbraith and J. A. Galbraith, "Super-resolution microscopy at a glance," *J Cell Sci,* vol. 124, no. 10, pp. 1607-1611, 15 May 2011.

[25] L. Schermelleh, H. Rainer and L. Heinrich, "A guide to super-resolution fluorescence microscopy," *The Journal of Cell Biology,* vol. 190, no. 2, pp. 165-175, 26 July 2010.

[26] B. Rieger, R. Nieuwenhuizen and S. Stallinga, "Image processing and analysis for single-molecule localization microscopy: Computation for nanoscale imaging," *IEEE Signal Processing Magazine,* vol. 32, no. 1, pp. 49-57, 2015.

[27] E. Betzig, G. H. Patterson, R. Sougrat, O. W. Lindwasser, S. Olenych, J. S. Bonifacino, W. D. Michael, L.-S. Jennifer and H. F. Hess, "Imaging intracellular fluorescent proteins at nanometer resolution," *Science,* vol. 313, no. 5793, pp. 1642-1645, 2006.

[28] I. Izeddin, J. Boulanger, V. Racine, C. G. Specht, A. Kechkar, D. Nair, A. Triller, D. Choquet, M. Dahan and J. B. Sibarita, "Wavelet analysis for single molecule localization microscopy," *Optics Express,* vol. 20, no. 3, pp. 2081-2095, 2012.

[29] A. L. McEvoy, D. Greenfield, M. Bates and J. Liphardt, "Q&A: Single-molecule localization microscopy for biological imaging," *BMC Biology,* vol. 8, no. 1, pp. 106, 2010.

[30] "About Image J," [Online]. Available: https://imagej.net/ImageJ. [Accessed 12 May 2017].

[31] G. T. Dempsey, J. C. Vaughan, K. H. Chen, M. Bates and X. Zhuang, "Evaluation of fluorophores for optimal performance in localization-based super-resolution imaging," *Nature Methods,* vol. 8, no. 12, pp. 1027–1036, November 2011.

[32] M. Ankerst, M. M. Breunig, K. Hans-Peter and J. Sander, "OPTICS: ordering points to identify the clustering structure," *ACM Sigmod Record,* vol. 28, no. 2, pp. 49-60, June 1999.

[33] F. Höppner, Fuzzy cluster analysis: methods for classification, data analysis and image recognition, John Wiley & Sons, pp. 8-9, 1999.

[34] E. Martin, K. Hans-Peter, J. Sander and X. Xiaowei., "A density-based algorithm for discovering clusters in large spatial databases with noise." KDD'96 Proceedings of the Second INternational Conference on Knowledge Dsicovery and Data Mining, August 02-04, 1996, vol. 96, no. 34, Portland, Oregon. Palo Alto, AAAI Press, 1996, pp. 226-231.

[35] J. Pi, S. Yong and C. Zhengxin, "Evaluation of cluster analysis algorithms enhanced by using R*-trees," in *Computer Systems and Applications, 2006. IEEE International Conference on*, 2008.

[36] P. Viswanath and R. Pinkesh., "l-dbscan: A fast hybrid density based clustering method," *Pattern Recognition, 2006. ICPR 2006. 18th International Conference on,* vol. 1, pp. 912-915, 2006.

[37] A. Hinneburg and D. A. Keim., "An efficient approach to clustering in large multimedia databases with noise." KDD'98 Proceedings of the Fourth International Conference on

Knowledge Discovery and Data Mining. August 27 - 31, 1998, vol. 98, New York, Palo Alto, AAAI Press, 1998, pp. 58-65.

[38] R. Boada, R. Borkowski and I. T. Monroy, "Clustering algorithms for Stokes space modulation format recognition," *Optic Express,* vol. 23, no. 12, pp. 15521-15531, 2015.

[39] C. Coltharp, X. Yang and J. Xiao, "Quantitative analysis of single-molecule superresolution images," *Current Opinion in Structural Biology,* vol. 28, pp. 112-121, 30 August 2014.

[40] T. Lagache, G. Lang, N. Sauvonnet and J.-C. Olivo-Marin, "Analysis of the spatial organization of molecules with robust statistics," *PLoS ONE,* vol. 8, no. 12, p. e80914, December 2013.

[41] M. A. Kiskowski, J. F. Hancock and A. K. Kenworthy, "On the use of Ripley's K-function and its derivatives to analyze domain size," *Biophysical Journal,* vol. 97, no. 4, pp. 1095–1103, 19 August 2009.

[42] A. Fürstenberg and M. Heilemann, "Single-molecule localization microscopy–near-molecular spatial resolution in light microscopy with photoswitchable fluorophores," *Physical Chemistry Chemical Physics,* vol. 15, no. 36, pp. 14919-14930, July 2013.

[43] F. Levet, E. Hosy, A. Kechkar, C. Butler, A. Beghin, D. Choquet and J.-B. Sibarita, "SR-Tesseler: a method to segment and quantify localization-based super-resolution microscopy data," *Nature Methods,* vol. 12, no. 11, pp. 1065–1071, 2015.

[44] P. Sengupta, T. Jovanovic-Talisman and J. Lippincott-Schwartz, "Quantifying spatial organization in point-localization superresolution images using pair correlation analysis," *Nature Protocols,* vol. 8, no. 2, pp. 345–354, 2013.

[45] B. Rieger, R. Nieuwenhuizen and S. Stallinga, "Image Processing and Analysis for Single-Molecule Localization Microscopy (Computation for nano scale imaging)," *IEEE Signal Processing Magazine,* vol. 32, no. 1, pp. 49-57, Janurary 2015.

[46] H.-P. Kriegel and P. Martin, "Hierachial density-based clustering of uncertain data". Data Mining, Fifth IEEE International Conference on, October 27-30, 2005, Houston, TX. Los Almitos, IEEE, 2006, pp. 22-24.

[47] M. S. Deepa and N. Sujatha, "Comparative Studies of Various Clustering Techniques and Its Characteristics," *International Journal of Advanced Networking and Applications,* vol. 5, no. 6, p. 2104, 2014.

[48] R. Klein., "Hierachial density-based clustering of uncertain data". Data Mining, Fifth IEEE International Conference on, November 27-30, 2005, Houston, TX. Los Almitos, IEEE, 2006, pp. 10-16.

[49] M. Senechal, "Spatial Tessellations: Concepts and Applications of Voronoi Diagrams," *Science,* vol. 260, no. 5111, pp. 1170-1173, 1993.

[50] F. Aurenhammer, "Voronoi diagrams—a survey of a fundamental geometric data structure," *ACM Computing Surveys (CSUR),* vol. 23, no. 3, pp. 345-405, 1991.

[51] Q. Mamun, "A tessellation-based localized chain construction scheme for chain-oriented sensor networks," *IEEE Sensors Journal,* vol. 13, no. 7, pp. 2648-2658, 2013.

[52] Y. Wang, P. Penkul and J. N. Milstein, "Quantitative localization microscopy reveals a novel organization of a high-copy number plasmid," *Biophysical Journal,* vol. 111, no. 3, pp. 467-479, 9 August 2016.

[53] S. Wolter, A. Löschberger, T. Holm, S. Aufmkolk, M.-C. Dabauvalle, S. Van De Linde and M. Sauer, "rapidSTORM: accurate, fast open-source software for localization microscopy," *Nature Methods,* vol. 9, no. 11, pp. 1040-1041, November 2012.

[54] A. Edelstein, A. Nenad, H. Karl, V. Ron and S. Nico, "Computer control of microscopes using μManager," *Current Protocols in Molecular Biology,* pp. 14-20, October 2010.

[55] "Download Micro-Manager Latest Release," 14 August 2015. [Online]. Available: https://micro-manager.org/wiki/Download%20Micro-Manager_Latest%20Release. [Accessed 20 March 2017].

[56] S. Ahmed, A. Chou, K. P. Sem, S. Thankiah, G. Wright, J. Lim and S. Hariharan, "Using dSTORM to probe the molecular architecture of filopodia," *Single Molecule Spectroscopy and Superresolution Imaging VII,* vol. 8950, p. 89500Y, 4 March 2014.

[57] Y. Wang, J. Schnitzbauer, Z. Hu, X. Li, Y. Cheng, Z.-L. Huang and B. Huang, "Localization events-based sample drift correction for localization microscopy with redundant cross-correlation algorithm," *Optics Express,* vol. 22, no. 13, pp. 15982-15991, 30 June 2014.

[58] B. Huang, W. Wang, M. Bates and X. Zhuang, "Three-dimensional super-resolution imaging by stochastic optical reconstruction microscopy," *Science,* vol. 319, no. 5864, pp. 810-813, 2008.

[59] L. Florian, H. Eric, K. Adel, B. Corey, B. Anne, C. Daniel and S. Jean-Baptiste, "SR-Tesseler: a method to segment and quantify localization-based super-resolution microscopy data," *Nature Methods,* vol. 12, pp. 1065–1071, September 2015.

[60] "MathWorks," 2016. [Online]. Available: https://www.mathworks.com/help/matlab/ref/voronoin.html. [Accessed 20 May 2016].

[61] W. R. Hill and D. M. Pillsbury, Argyria: the pharmacology of silver, Williams & Wilkins Company, 1939.

[62] M. Heger, "A Silver Coating in the Fight Against Microbes," 2 May 2008. [Online]. Available: https://www.scientificamerican.com/article/silver-coating-fights-microbes. [Accessed 15 April 2017].

[63] S. Wang, L. Zhoujun, C. Wenhan and C. Qinghua., "Applying adaptive over-sampling technique based on data density and cost-sensitive SVM to imbalanced learning". Neural Networks (IJCNN), The 2012 International Joint Conference on, June 10-15, 2012, Brisbane, QLD, Australia. Los Alamitos, IEEE Press, 2012.

Appendix A. Description of Research for Popular Publication

Can Silver Metal be Used as an Antibiotic?

Microbes are present everywhere around the earth. While most of the microbes are harmless, some can cause serious diseases. To prevent the microbes from causing the diseases, silver metal was used as an antibiotic. Silver was the third metal used by the ancients, after gold and copper, since 4,000 B.C.E [1]. Greeks, Romans, and Egyptians used silver as a preservative agent for storing food [1]. In olden days when there were no refrigerators, water and milk was preserved by dropping the silver coins in the vessels, unaware of the fact that silver could suppress the formation and growth of bacteria that causes infections. Silver foils were used to cure wounds and prevent infections [1]. Royal families used silverware for cooking and dining purposes for maintaining good health. Silver was used to cure various infections and noninfectious diseases. As per the survey of U.S Centers for Disease Control and Prevention (CDC) most people are affected by bacterial infections [1].

In recent years, bacteria has gained resistance to antibiotics and it has become a serious issue in the field of medicine. To address this problem, research has been carried out at the University of Arkansas on silver ions as antibiotics to suppress bacteria growth. From past decades, silver didn't show any opposing effect on humans. To know whether silver metal can really suppress the growth and formation of bacteria, experiments were carried out on Histone Like Nucleoid Structuring Proteins (*H-NS*) in *E. coli* bacteria. With the help of Super Resolution Microscopy, the samples were analyzed. The images below indicate that silver ions really help in suppression and cluster formation of H-NS Proteins which reveal the fact that silver ions have a positive impact on the bacterial growth suppression. In the future, silver might help to handle other health issue problems.

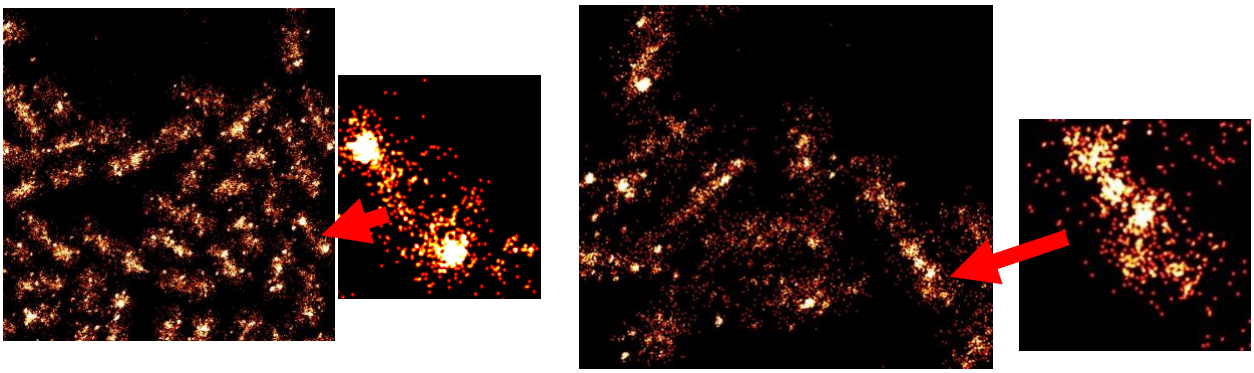

Figure 1. The Visual Effect of Silver Ions on the Organization of H-NS Proteins.

Reference:

1. A. J. Wesley, "History of the medical use of silver," *Surgical infections*, vol. 10, no. 3, pp. 289-292, 2009.

Appendix B. Executive Summary of Newly Created Intellectual Property

The following items were developed during this research project and should be considered for intellectual property.

1. A MATLAB script to identify cluster formation in input data based on a density criteria to differentiate from other clusters present in the data.
2. A MATLAB script to perform Voronoi analysis on input data to understand the physical limits of organization of proteins.

Appendix C. Potential Patent and Commercialization Aspects of listed Intellectual Property Items

C.1. Patentability of Intellectual Property

1. The MATLAB script to identify cluster formation is not patentable because the idea is not new. However, no open source code is available and the code was written specially for this research project.
2. The MATLAB script to perform Voronoi analysis computational method is not patentable because the idea is not new. However, no open source code is available and the code was written specially for this research project.

C.2. Commercialization Prospects (Should Each Item Be Patented)

The algorithm should not be patented as it can be decoded by an expert who has command in coding language.

C.3. Possible Prior Disclosure of IP

The algorithm was discussed in MicroEP community during Research Communications Seminar in the Spring 2016 semester and in presentations. The following is a list of Presentations.

1. Presented Poster at 76th Physical Electronics Conference (PEC) June 20-23, 2016.
2. Presented Poster at Arkansas Academy of Science (AAC) conference April 1-2, 2016.
3. Presented Poster at Industrial Advisory Board Annual Poster presentation. October 23, 2016.

Appendix D. Broader Impact of Research

D.1. Applicability of Research Methods to Other Problems

As silver ions had a positive impact in suppression of bacteria growth, researchers say that silver might solve the problem of drug companies in discovery of new drugs to replace old antibiotics drugs which bacteria have become resistant to. The advantages of using Voronoi and cluster analysis algorithms are their robustness and performance on simulated and real data. Clustering algorithms might open doors for implementation of these algorithms in analyzing and solving several problems in fields as engineering, medicine, geology etc. Clustering and Voronoi analysis are applied in the field of medicine in understanding the fundamental biological information of organisms.

D.2. Impact of Research Results on U.S. and Global Society

Silver metal is playing a crucial in the field of medicine for inventing new antibiotics. In this way, the disease spreading bacteria can be suppressed and the rate of people falling sick can be reduced. In the past few years, disease causing bacteria are gaining resistance against antibiotics and are becoming less effective. Due to this, the intake of medicines is increasing and medical expenses are increasing rapidly. With the implementation of clustering algorithms, the reaction of bacteria to antibiotics can be analyzed. This will be a great step in the invention of new antibiotics that can cure and prevent various diseases and improve people's health. In this way, the cost of medical expenses can also be reduced.

D.3. Impact of Research Results on the Environment

The research was carried out in a wet lab and does not possess a significant impact on the environment. The experiments are performed in the lab are done using petri dishes and culture

tubes; samples were prepared on the coverslips and slides and imaged using super resolution microscopy. Although, silver compounds play in important role as antibiotics, they pose a serious threat when intake is at higher dosage in animals and humans. If silver compounds are exposed to sunlight they turn to silver metal [1]. The metal usually deposits as microscopic particles in the skin causing a disease called argyria [1].

References

1. James, W. D., Berger, T. G., Elston, D. M., and Odom, R. B. *Andrews' Diseases of the Skin: Clinical Dermatology*. Saunders Elsevier. 2006. p. 858.

Appendix E. Microsoft Project for MS MicroEP Degree Plan

Task Name	Duration	Start	Finish	Predecessors	Resou
Joining MICROEP	1 day	Tue 8/11/15	Tue 8/11/15		
Select Professor	31 days	Thu 9/3/15	Thu 10/15/15		
Check Website	23 days	Thu 9/3/15	Mon 10/5/15		
Talk to Students	17 days	Wed 9/9/15	Thu 10/1/15		
Talk to professors	6 days?	Mon 2/8/16	Mon 2/15/16	4	
Courses	530 days	Mon 8/17/15	Thu 8/17/17		
ELAC 4043	81 days	Mon 8/24/15	Mon 12/14/15		
ELAC 0011	77 days	Tue 8/25/15	Wed 12/9/15		
ELEG 5203	83 days?	Tue 8/25/15	Thu 12/17/15		
MEPH 5811	66 days?	Mon 8/31/15	Mon 11/30/15		
MEPH 5911	1 day?	Mon 8/17/15	Mon 8/17/15		
PHYS 5773	83 days?	Wed 1/20/16	Thu 5/12/16		
MEPH 5383	81 days?	Tue 1/19/16	Mon 5/9/16		
MEPH 6811	71 days?	Tue 8/30/16	Mon 12/5/16		
STAT 4101L	54 days?	Thu 8/25/16	Mon 11/7/16		
ELEG 5213	83 days?	Wed 8/24/16	Thu 12/15/16		
MEPH 5821	47 days?	Fri 6/3/16	Thu 8/4/16		
MEPH 5611	65 days?	Wed 9/7/16	Mon 12/5/16		
ELEG5213	89 days?	Tue 8/16/16	Thu 12/15/16		
PHYS 600V	62 days?	Fri 5/13/16	Thu 8/4/16		
Submitted a summary paper about my rese	21 days?	Mon 7/4/16	Sat 7/30/16		
MEPH 6911	89 days?	Mon 1/9/17	Tue 5/9/17		
ELEG 5293L	88 days?	Tue 1/17/17	Wed 5/17/17		
ELEG 587V	87 days?	Wed 1/18/17	Wed 5/17/17		
PHYS 3613	81 days?	Mon 8/22/16	Fri 12/9/16		
Thesis Title Submission	1 day?	Tue 5/10/16	Tue 9/6/16		
Form thesis comittie	1 day?	Mon 3/14/16	Mon 3/14/16		
Determine Research Topic	1 day?	Thu 3/10/16	Thu 3/10/16		
Research Document	1 day	Tue 3/15/16	Tue 3/15/16	27	
Preparation Of Poster	2 days	Wed 3/30/16	Thu 3/31/16		
AAS Poster Presentation	1 day	Sat 4/2/16	Sat 4/2/16		

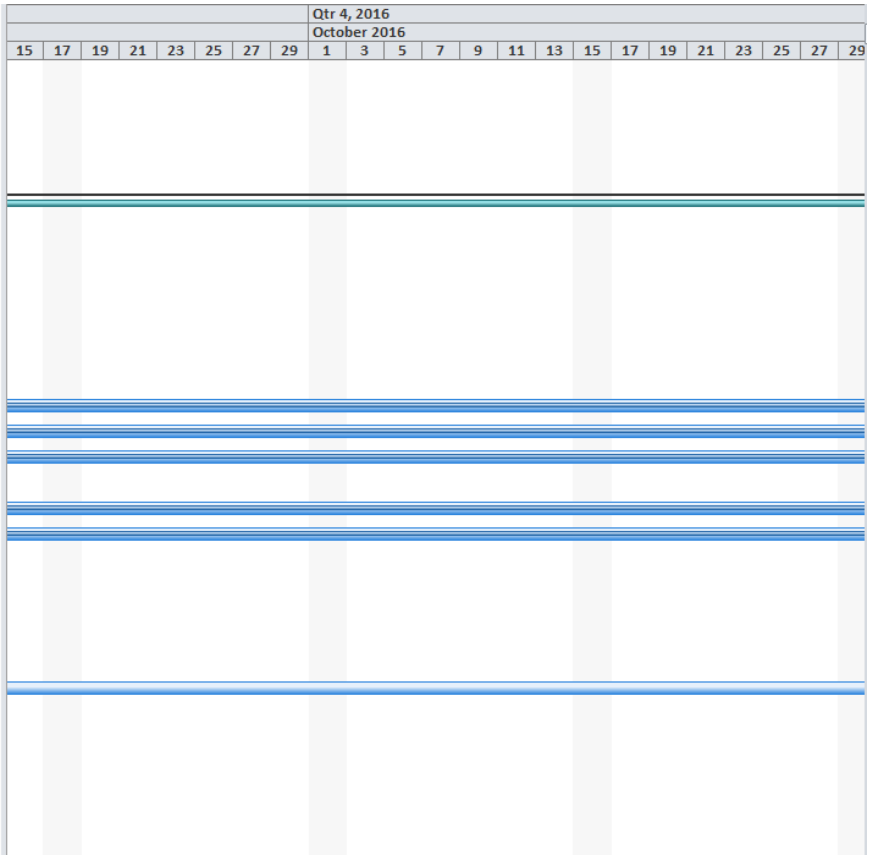

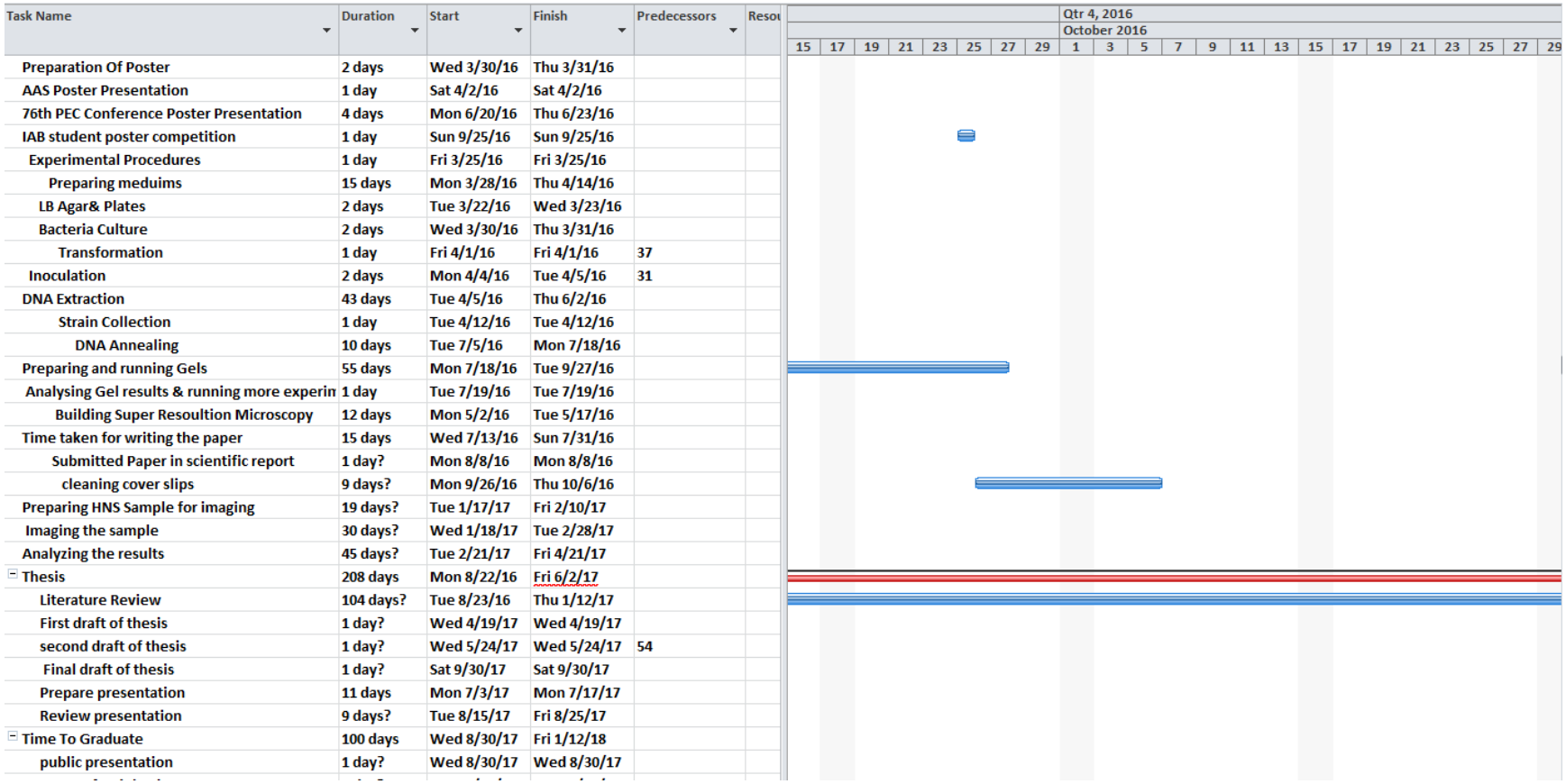

Task Name	Duration	Start	Finish	Predecessors	Resou
Preparation Of Poster	2 days	Wed 3/30/16	Thu 3/31/16		
AAS Poster Presentation	1 day	Sat 4/2/16	Sat 4/2/16		
76th PEC Conference Poster Presentation	4 days	Mon 6/20/16	Thu 6/23/16		
IAB student poster competition	1 day	Sun 9/25/16	Sun 9/25/16		
Experimental Procedures	1 day	Fri 3/25/16	Fri 3/25/16		
Preparing meduims	15 days	Mon 3/28/16	Thu 4/14/16		
LB Agar& Plates	2 days	Tue 3/22/16	Wed 3/23/16		
Bacteria Culture	2 days	Wed 3/30/16	Thu 3/31/16		
Transformation	1 day	Fri 4/1/16	Fri 4/1/16	37	
Inoculation	2 days	Mon 4/4/16	Tue 4/5/16	31	
DNA Extraction	43 days	Tue 4/5/16	Thu 6/2/16		
Strain Collection	1 day	Tue 4/12/16	Tue 4/12/16		
DNA Annealing	10 days	Tue 7/5/16	Mon 7/18/16		
Preparing and running Gels	55 days	Mon 7/18/16	Tue 9/27/16		
Analysing Gel results & running more experin	1 day	Tue 7/19/16	Tue 7/19/16		
Building Super Resoultion Microscopy	12 days	Mon 5/2/16	Tue 5/17/16		
Time taken for writing the paper	15 days	Wed 7/13/16	Sun 7/31/16		
Submitted Paper in scientific report	1 day?	Mon 8/8/16	Mon 8/8/16		
cleaning cover slips	9 days?	Mon 9/26/16	Thu 10/6/16		
Preparing HNS Sample for imaging	19 days?	Tue 1/17/17	Fri 2/10/17		
Imaging the sample	30 days?	Wed 1/18/17	Tue 2/28/17		
Analyzing the results	45 days?	Tue 2/21/17	Fri 4/21/17		
Thesis	208 days	Mon 8/22/16	Fri 6/2/17		
Literature Review	104 days?	Tue 8/23/16	Thu 1/12/17		
First draft of thesis	1 day?	Wed 4/19/17	Wed 4/19/17		
second draft of thesis	1 day?	Wed 5/24/17	Wed 5/24/17	54	
Final draft of thesis	1 day?	Sat 9/30/17	Sat 9/30/17		
Prepare presentation	11 days	Mon 7/3/17	Mon 7/17/17		
Review presentation	9 days?	Tue 8/15/17	Fri 8/25/17		
Time To Graduate	100 days	Wed 8/30/17	Fri 1/12/18		
public presentation	1 day?	Wed 8/30/17	Wed 8/30/17		

Task Name	Duration	Start	Finish	Predecessors	Resou
Preparing meduims	15 days	Mon 3/28/16	Thu 4/14/16		
LB Agar& Plates	2 days	Tue 3/22/16	Wed 3/23/16		
Bacteria Culture	2 days	Wed 3/30/16	Thu 3/31/16		
Transformation	1 day	Fri 4/1/16	Fri 4/1/16	37	
Inoculation	2 days	Mon 4/4/16	Tue 4/5/16	31	
DNA Extraction	43 days	Tue 4/5/16	Thu 6/2/16		
Strain Collection	1 day	Tue 4/12/16	Tue 4/12/16		
DNA Annealing	10 days	Tue 7/5/16	Mon 7/18/16		
Preparing and running Gels	55 days	Mon 7/18/16	Tue 9/27/16		
Analysing Gel results & running more experin	1 day	Tue 7/19/16	Tue 7/19/16		
Building Super Resoultion Microscopy	12 days	Mon 5/2/16	Tue 5/17/16		
Time taken for writing the paper	15 days	Wed 7/13/16	Sun 7/31/16		
Submitted Paper in scientific report	1 day?	Mon 8/8/16	Mon 8/8/16		
cleaning cover slips	9 days?	Mon 9/26/16	Thu 10/6/16		
Preparing HNS Sample for imaging	19 days?	Tue 1/17/17	Fri 2/10/17		
Imaging the sample	30 days?	Wed 1/18/17	Tue 2/28/17		
Analyzing the results	45 days?	Tue 2/21/17	Fri 4/21/17		
Thesis	208 days	Mon 8/22/16	Fri 6/2/17		
Literature Review	104 days?	Tue 8/23/16	Thu 1/12/17		
First draft of thesis	1 day?	Wed 4/19/17	Wed 4/19/17		
second draft of thesis	1 day?	Wed 5/24/17	Wed 5/24/17	54	
Final draft of thesis	1 day?	Sat 9/30/17	Sat 9/30/17		
Prepare presentation	11 days	Mon 7/3/17	Mon 7/17/17		
Review presentation	9 days?	Tue 8/15/17	Fri 8/25/17		
Time To Graduate	100 days	Wed 8/30/17	Fri 1/12/18		
public presentation	1 day?	Wed 8/30/17	Wed 8/30/17		
Defend thesis	1 day?	Mon 9/11/17	Mon 9/11/17		
Send all documents to Microep	1 day?	Wed 10/18/17	Wed 10/18/17		
Final Submission	3 days?	Wed 10/25/17	Fri 10/27/17		
DEAD DAY	1 day?	Sat 12/16/17	Sat 12/16/17	63	

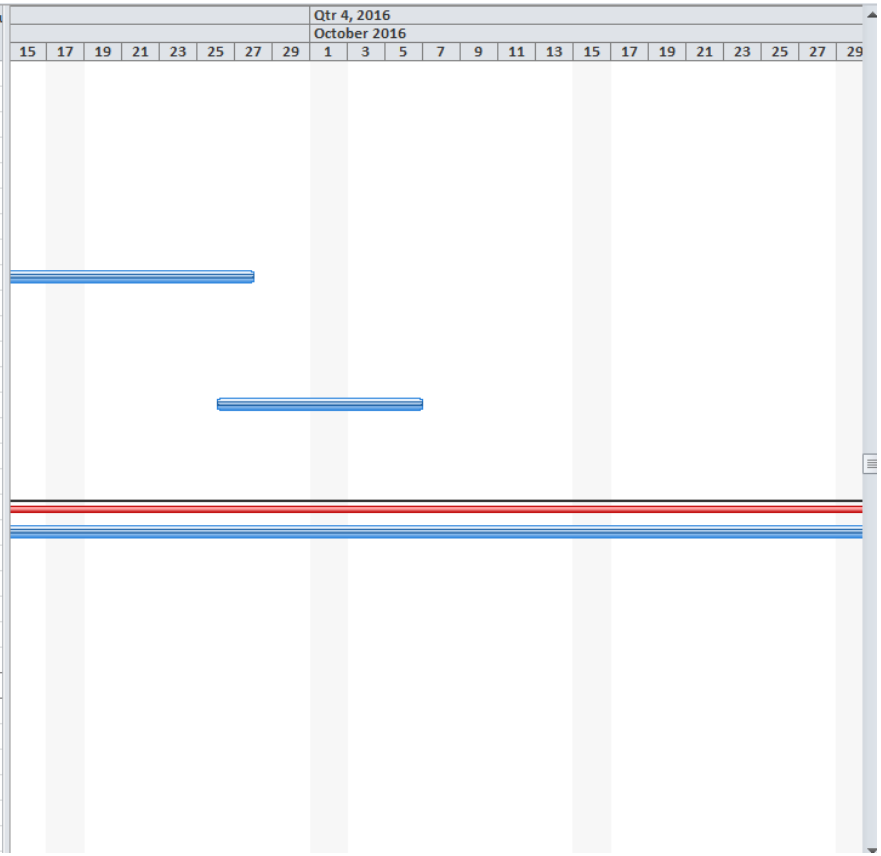

Appendix F. Identification of All Software Used in Research and Thesis Generation

Computer #1:
Model Number : Mac book Pro
Serial Number : C02P2SD6G3QJ
Location : N/A
Owner : Challapalli Sai Divya

Software #1:
Name : Microsoft Office 365
Owner : Challapalli Sai Divya

Software #2:
Name : MATLAB R2016b (Version 9.1)
Owner : University of Arkansas Department Physics

Software #3:
Name : ImageJ (Version 2.0)
Owner : Open source image processing software

Computer #2:
Model Number : N/A (Custom built)
Serial Number : N/A (Custom built)
Location : PHYS 115A
Owner : Dr. Yong Wang

Software #1:
Name : Micro-Manager
Owner : Freeware

Software #2:
Name : rapidSTORM
Owner : Freeware

Software #3:
Name : MATLAB R2016b (Version 9.1)
Owner : University of Arkansas Department Physics

Software #3:
Name : Image J
Owner : Open source image processing software

Appendix G. All Publications Published, Submitted and Planned

Journal Publications

- Jiang S, Park S, Challapalli SD, Fei J, Wang Y (2017) Robust nonparametric quantification of clustering density of molecules in single-molecule localization microscopy. *PLoS ONE*, vol. 12, no. 6, P. e0179975, 2015.